Published in final edited form as:

Neuron. 2021 December 15; 109(24): 3962–3979.e6. doi:10.1016/j.neuron.2021.09.040.

Genome Instability Independent of Type I Interferon Signaling Drives Neuropathology Caused by Impaired Ribonucleotide Excision Repair

Aditi[1], **Susanna M. Downing**[1], **Patrick A. Schreiner**[2], **Young Don Kwak**[1], **Yang Li**[1], **Timothy I. Shaw**[3], **Helen R. Russell**[1], **Peter J. McKinnon**[1,4,5]

[1]Center for Pediatric Neurological Disease Research, St. Jude Pediatric Translational Neuroscience Initiative, Dept. Cell Mol. Biology, St. Jude Children's Research Hospital, Memphis, TN, USA.

[2]Center for Applied Bioinformatics, St. Jude Children's Research Hospital, Memphis, TN, USA.

[3]Moffit Cancer Center, Tampa, Florida, St. Jude Children's Research Hospital, Memphis, TN, USA.

[4]St. Jude Graduate School of Biomedical Sciences, St. Jude Children's Research Hospital, Memphis, TN, USA.

Abstract

Aicardi-Goutières syndrome (AGS) is a monogenic type I interferonopathy characterized by neurodevelopmental defects and upregulation of type I interferon signaling and neuroinflammation. Mutations in genes that function in nucleic acid metabolism, including *RNASEH2* are linked to AGS. Ribonuclease H2 (RNASEH2) is a genome surveillance factor critical for DNA integrity by removing ribonucleotides incorporated into replicating DNA. Here we show that RNASEH2 is necessary for neurogenesis and to avoid activation of interferon-responsive genes and neuroinflammation. Cerebellar defects after RNASEH2B inactivation are rescued by p53 but not cGAS deletion, suggesting that DNA damage signaling, not neuroinflammation, accounts for neuropathology. Coincident inactivation of *Atm* and *Rnaseh2* further impacted cerebellar development causing ataxia, which was dependent upon aberrant activation of non-homologous end-joining (NHEJ). The loss of ATM also markedly exacerbates cGAS-dependent type I interferon signaling. Thus, DNA damage-dependent signaling rather than type I interferon signaling underlies neurodegeneration in this class of neurodevelopmental/neuroinflammatory disease.

eTOC.

[5] Lead contact: peter.mckinnon@stjude.org.

Author contributions.

A., S.M.D. and P.J.M. conceived and planned experiments and produced the final version of the manuscript. Y-D.K. performed in vivo TOP1cc analysis. S.M.D., T.I.S. and P.A.S. provided bioinformatics analysis of RNA-seq experiments. A. and Y.L. performed histology, immunostaining and tissue collection. A. and H.R.R. generated the mutant mouse models and performed additional experiments. All authors contributed to editing and completion of the manuscript.

Declaration of interests.

The authors have nothing to declare.

Mutations in *RNASEH2* are linked to Aicardi-Goutières syndrome. Aditi et. al., show that RNASEH2 is necessary for neurogenesis and to avoid activation of interferon-responsive genes. These defects are rescued by p53 but not cGAS inactivation, suggesting that DNA damage signaling, not neuroinflammation, accounts for neuropathology in this class of disease.

Introduction.

Innate immune sensing of nucleic acids is a fundamental mechanism to restrict pathogen infection and maintain tissue homeostasis (Hu and Shu, 2018; Rankin and Artis, 2018; Tan et al., 2018). To prevent aberrant recognition of self-DNA, various checkpoints ensure that the immune system is not unduly activated (Bartok and Hartmann, 2020). However, accumulation of DNA damage due to inadequate DNA repair results in genomic instability, senescence and expression of inflammatory molecules that could subsequently lead to engagement of the immune system (Nakad and Schumacher, 2016; Nastasi et al., 2020; Xu, 2006). The interactions between DNA damage signaling and the immune system are tightly coordinated to mount an appropriate response in a context-specific manner, while its dysregulation leads to various inflammation-associated human disorders such as, Aicardi-Goutières syndrome (AGS) (Hu and Shu, 2020; Roers et al., 2016; Uggenti et al., 2019).

AGS is an early onset childhood neuroinflammatory disorder that mimics congenital viral infection and is associated with elevated type I interferon immune signaling. AGS primarily affects brain and skin and is characterized by encephalopathy involving microcephaly, seizures, intracranial calcification, white matter abnormalities and chilblain skin lesions (Aicardi and Goutieres, 1984; Crow et al., 2015; Crow and Manel, 2015; Livingston and Crow, 2016). Enhanced interferon-alpha (IFN-α) levels in the cerebrospinal fluid (CSF) and serum is a hallmark feature of this disease (Lebon et al., 1988; Rice et al., 2013). Thus, AGS is considered a ‘type I interferonopathy where enhanced type I IFN induction is implicated in disease manifestation (Crow, 2011; Lee-Kirsch, 2017); however, the pathogenic role of IFN-α in AGS remains uncertain.

AGS is associated with mutations in 7 different genes, all of which function in nucleic acid metabolism; *TREX1, RNASEH2A, RNASEH2B, RNASEH2C, SAMHD1, IFIH1,* and *ADAR1* (Crow et al., 2006a; Crow et al., 2006b; Rice et al., 2009; Rice et al., 2014; Rice et al., 2012). Mutations in *RNASEH2* accounts for more than 50% of AGS cases (Crow et al., 2015). RNASEH2 is a heterotrimeric complex consisted of catalytic RNASEH2A and accessory subunits RNASEH2B and RNASEH2C (Cerritelli and Crouch, 2009; Jeong et al., 2004). The accessory subunits mediate protein-protein interactions and/ or promote complex assembly and the RNASEH2 complex requires all three subunits for its function (Chon et al., 2009; Reijns et al., 2011). RNASEH2 functions as a genome surveillance factor to remove ribonucleotides embedded in the DNA. This occurs via an incision 5’ of the ribonucleotide followed by strand displacement synthesis, excision of the flap and then ligation, a process known as ribonucleotide excision repair (Hiller et al., 2012; Reijns et al., 2012; Sparks et al., 2012; Williams and Kunkel, 2014). RNASEH2 can also resolve RNA-DNA hybrids such as those found in R-loops (Amon and Koshland, 2016). Murine germline *Rnaseh2* deletion is embryonic lethal, leading to a p53-dependent DNA damage response (Hiller et al., 2012;

Reijns et al., 2012; Uehara et al., 2018). Although AGS-linked *RNASEH2* mutations are proposed to reduce protein function/stability and mislocalization (Chon et al., 2009; Perrino et al., 2009; Reijns et al., 2011; Rohman et al., 2008), how these mutations contribute to disease phenotype are unclear. Studies using RNASEH2 mouse models of AGS have shown that Cyclic GMP-AMP synthase (cGAS)- Stimulator of interferon genes (STING) innate immune pathway is required for type I IFN activation (Mackenzie et al., 2016; Pokatayev et al., 2016). While these models yielded important insight into disease immunology, they fail to recapitulate the nervous system defects characteristic of AGS, despite type I IFN induction.

Defective DNA repair causing damage accumulation are central features of many human neurological syndromes, suggesting a clear vulnerability of the nervous system towards compromised genome stability (McKinnon, 2013, 2017). Chronic DNA damage is a key feature of RNASEH2 deficiency (McKinnon, 2017; Reijns et al., 2012; Williams et al., 2016), suggesting this might also contribute importantly towards the neurological phenotype of AGS. To investigate the functions of RNASEH2 in the nervous system and decipher if DNA damage and/or type I IFN signaling drives AGS neuropathology, we generated a murine model of neural *Rnaseh2b* inactivation. Contrary to previous findings, we show that loss of RNASEH2 function leads to cerebellar atrophy, white matter defects and neuroinflammation, mirroring AGS. Remarkably, coincident loss of ATM dramatically worsened the neuropathology, neuroinflammation and these mice also develop ataxia. Additionally, abrogation of p53-dependent DNA damage signaling rescues the neurodegeneration, even though RNASEH2-p53 deleted cells have heightened type I IFN signaling. Taken together, our data suggests that it is unrepaired DNA damage that triggers neurodegeneration, which occurs independent of type I IFN, thus delineating a key mechanistic aspect of AGS.

Results.

RNASEH2 deficiency causes neurodevelopment defects similar to AGS.

AGS-linked hypomorphic *Rnaseh2* mutations mainly affect the nervous system (Crow and Manel, 2015; Livingston and Crow, 2016), but why this tissue is particularly sensitive to RNASEH2 loss is unclear. To investigate RNASEH2 function in the nervous system we used Nestin-cre, which expresses throughout neuroprogenitors from embryonic day 11 (E11). Effective *Rnaseh2b* deletion was confirmed by qPCR and genomic PCR, respectively (Figure S1A, S1B & S1C). In contrast to embryonic lethality observed in germline $Rnaseh2b^{-/-}$ animals, $Rnaseh2b^{LoxP/LoxP}$;*Nestin-Cre* (hereafter $Rnaseh2b^{Nes\text{-}cre}$), mice were viable, fertile and did not show any gross behavioral phenotype (Figure S1D), although they did exhibit sporadic seizures. Analysis of the $Rnaseh2b^{Nes\text{-}cre}$ brain showed a smaller cerebellum with thinning of the inner granule layer, particularly in the anterior lobules (Figure 1A &1B). Magnetic resonance imaging (MRI) revealed a significantly smaller cerebellar volume in $Rnaseh2b^{Nes\text{-}cre}$ (21% smaller) compared to control (Figure 1C). Although overall $Rnaseh2b^{Nes\text{-}cre}$ cerebellar morphology was intact, H&E analysis indicated a clear loss of granule neurons and interneurons (Figure 1D & S1E). In contrast, cerebellar Purkinje cells and oligodendrocytes were not obviously affected in the $Rnaseh2b^{Nes\text{-}cre}$

cerebellum as visualized by normal CA8 and CNPase immunostaining (Figure 1E). Further, in contrast to a reduced granule layer in the *Rnaseh2b*$^{Nes\text{-}cre}$ cerebellum, measurement of the molecular layer showed no difference between controls and the mutant, supporting a lack of effect towards Purkinje cells after RNASEH2B inactivation (Figure S1E). While overall cortex size was unaffected, the dentate gyrus was smaller and acellular compared to control brains (Figure S1F & S1G).

Identification of oligodendrocytes using Olig2 showed thinning of the corpus callosum and loss of oligodendrocytes in *Rnaseh2b*$^{Nes\text{-}cre}$ brains, consistent with these features in AGS (Abdel-Salam et al., 2004) (Figure 1G). However, myelination in the cortex or hippocampus was not markedly perturbed (Figure S1G, S1H &S1I), and elsewhere there were no significant changes in Olig2+ cell numbers (Figure S1I). Furthermore, MRI-diffusion tensor imaging (DTI) of the corpus callosum region using fractional anisotropy showed a 10% reduction ($p=0.0008$) in the adult *Rnaseh2b*$^{Nes\text{-}cre}$ brains (Figure 1H). Because DTI is a sensitive method to determine the microstructural changes, our data indicates white matter irregularities occur in the *Rnaseh2b*$^{Nes\text{-}cre}$ brain, similar to AGS.

We next utilized RNA-seq to determine the gene expression changes in the *Rnaseh2b*$^{Nes\text{-}cre}$ cerebellum and compared the transcriptome of 7 control and 7 mutant adult cerebella. Consistent with histology data, gene set enrichment (GSEA) analysis showed underrepresentation of genes related to granule neurons and interneurons in *Rnaseh2b*$^{Nes\text{-}cre}$ cerebellum (Figure 1F & Table S1). This phenotype is reminiscent of XRCC1 loss (a base excision repair factor), which also results in the loss of cerebellar interneurons and granule cells (Lee et al., 2009).

Finally, we determined if the smaller cerebellar size of *Rnaseh2b*$^{Nes\text{-}cre}$ is due to DNA damage-induced cell death. An increased number of γH2AX (a marker for DNA double-strand breaks) positive cells were seen during early cerebellar development and in other regions of the *Rnaseh2b*^{Nes}-cre brain (Figure 1I and Figure S1J). Notably, γH2AX staining was observed in the external granule layer (EGL) of the P5 *Rnaseh2b*$^{Nes\text{-}cre}$ cerebellum and overlapped with the proliferation marker, PCNA (Figure 1I). We did not observe γH2AX immunostaining in the adult cerebellum (at P28 and 6 months of age; data not shown), suggesting DNA damage from RNASEH2 loss predominately affects proliferating cells. These results are consistent with a critical role of RNASEH2 during DNA replication. Enhanced TUNEL staining coincided with DNA damage in the P5 *Rnaseh2b*$^{Nes\text{-}cre}$ cerebellum, indicative of cell death (Figure 1J). Interestingly, we observed increased TUNEL positive cells in the anterior *Rnaseh2b*$^{Nes\text{-}cre}$ cerebellar lobules (I-V), indicating disproportionate neuronal loss. Thus, widespread DNA damage-dependent cell death of granule neurons may account for the smaller *Rnaseh2b*$^{Nes\text{-}cre}$ cerebellar size.

Activation of type I interferon and altered astrocyte and microglia specific gene expression occur in the *Rnaseh2b*$^{Nes\text{-}cre}$ cerebellum.

A hallmark feature of AGS is the activation of a type I interferon response and neuroinflammation. However, available AGS mouse models such as *Trex1*$^{-/-}$, *Rnaseh2b*$^{A174T/A174T}$, *Rnaseh2*$^{\Delta GFAP}$, *Samhd1*$^{-/-}$ fail to show a type I interferon response or inflammation in the brain (Bartsch et al., 2018; Behrendt et al., 2013; Mackenzie et

al., 2016; Morita et al., 2004; Peschke et al., 2016; Rehwinkel et al., 2013). Therefore, we investigated if a neuroinflammatory signature is also present in *Rnaseh2b*$^{Nes\text{-}cre}$ mice. Analysis of RNA-seq data (Figure 1) showed ~170 genes were differentially expressed in *Rnaseh2b*$^{Nes\text{-}cre}$ cerebellum compared to control (FDR <0.05) (Figure 2A, S2A & Table S2). Notably, several immune function related genes including *Il21r* and *Ifi44* were significantly upregulated in *Rnaseh2*$^{Nes\text{-}cre}$ cerebella (Figure 2A & Table S2). Ingenuity Pathway Analysis (IPA) to identify signaling networks affected in the *Rnaseh2b*$^{Nes\text{-}cre}$ cerebellum showed immune related pathways such as “activation of antigen presenting cells” and “cytotoxicity of lymphocytes” etc. as a major theme in the core analysis (Figure S2B). We then performed GSEA analysis to determine if type I IFN signaling is activated. Strikingly, GSEA analysis showed significant enrichment of type I interferon alpha response pathway genes (Figure 2B & Table S1), which was confirmed using RT-PCR to show transcriptional increase of *Ifit1*, *Ifit3*, *Isg15*, *Igtp* and *Irf7* interferon-stimulated genes in the *Rnaseh2b*$^{Nes\text{-}cre}$ cerebellum (Figure 2C). Thus, contrary to previous findings (Bartsch et al., 2018; Mackenzie et al., 2016; Pokatayev et al., 2016), our data clearly indicate that RNASEH2 deficiency in the brain stimulates the induction of a type I interferon response.

Astrocytes are important inducers of neuroinflammation in AGS (Sase et al., 2018; van Heteren et al., 2008). Accordingly, we observed astrocyte-specific genes such as *Gfap* and *Aqp4*, as the top differentially expressed genes in the *Rnaseh2b*$^{Nes\text{-}cre}$ cerebellum (Figure S2A & Table S2). Importantly, we identified cell-type enrichment via single sample GSEA, which demonstrated elevated astrocyte and microglia enriched genes in *Rnaseh2b*$^{Nes\text{-}cre}$ cerebellum compared to control (Figure 2D & Table S1). While the RNA-seq samples represent a mixture of cell types in the brain, identification of enriched cell subtypes was derived from analysis using five independent human and mouse datasets (McKenzie et al., 2018), resulting in assignment of the top ranked cell type-enriched genes for the six cell types shown in Fig 2D.

Consistent with transcriptomics data, immunohistochemical analysis of adult cerebellum revealed increased astrocytosis as shown by significantly increased *Gfap* message and protein (Figure 2E & 2F), and microglia activation markers Iba1 (Figure 2G). Thus, *Rnaseh2* inactivation in the brain causes an AGS-like inflammatory response.

RNASEH2 loss promotes the accumulation of cytoplasmic DNA damage.

Accumulation of DNA damage is known to stimulate an inflammatory response through innate immune signaling (Kellner and Luke, 2020; Nakad and Schumacher, 2016; Nastasi et al., 2020; Xu, 2006). As our data indicates neuroinflammation occurs in *Rnaseh2b*$^{Nes\text{-}cre}$ mice, we next asked the nature of DNA damage present that primes the type I interferon response. To investigate this, we isolated primary cortical astrocytes and neural stem cells from *Rnaseh2b*$^{Nes\text{-}cre}$ brains. Like reports showing RNASEH2 is essential for proliferation (Hiller et al., 2012; Reijns et al., 2012), RNASEH2-deleted astrocytes and neural stem cells failed to thrive in culture (Figure S3A, S3B & S3C). Beta-galactosidase staining revealed that RNASEH2-deleted astrocytes underwent premature senescence (Figure S3D) and accumulated significant DNA damage as visualized by γH2AX and phospho-KAP1

(Figure S3E). Thus, the deletion of RNASEH2 in neural cells leads to DNA damage-induced senescence.

Growth of RNASEH2-deleted cells can be rescued by p53 inactivation (Hiller et al., 2012; Reijns et al., 2012). However, after a few passages, (*Rnaseh2b;p53)*$^{Nes\text{-}cre}$ astrocytes grew slower compared to *p53*$^{Nes\text{-}cre}$ astrocytes (Figure S3F & S3G). Immunostaining using DNA damage markers showed a significant accumulation of DNA damage in (*Rnaseh2b;p53*)$^{Nes\text{-}cre}$ compared to *p53*$^{Nes\text{-}cre}$ astrocytes (Figure S3H), and a significant increase in the number of multinucleated cells with abnormal morphology in addition to cells with micronuclei (Figure 3A). Given the similar cerebellar interneuron phenotype of *Rnaseh2b*$^{Nes\text{-}cre}$ and *Xrcc1*$^{Nes\text{-}cre}$ mice, we determined if *Xrcc1*-null astrocytes also form multinucleated cells. We did not observe a significant accumulation of multinucleated cells in (*Xrcc1;p53*)$^{Nes\text{-}cre}$ astrocytes (Figure 3A), indicating a distinct function for RNASEH2 is preventing the multinucleated phenotype. RNASEH2 also removes embedded genomic ribonucleotides via ribonucleotide excision repair and prevents R-loop accumulation. Alkaline gel electrophoresis revealed an enhanced accumulation of ribonucleotides in the DNA in the (*Rnaseh2b;p53)*$^{Nes\text{-}cre}$ astrocytes (Figure 3B). We also observed an increase in R-loops in the nucleus in (*Rnaseh2b;p53*)$^{Nes\text{-}cre}$ astrocytes, as measured by S9.6 immunostaining that detects RNA/DNA hybrids (Figure S3I).

Genomic ribonucleotides can also be removed by topoisomerase I (Sekiguchi and Shuman, 1997). However, repair of ribonucleotides by topoisomerase I is error-prone and results in the formation of covalent Top1-DNA covalent complexes (Top1cc) (Kellner and Luke, 2020; Kim et al., 2011; Pommier et al., 2016). Immunostaining with a Top1cc-specific antibody (Patel et al., 2016), showed enhanced Top1cc formation in (*Rnaseh2b;p53)*$^{Nes\text{-}cre}$ astrocytes compared to control (Figure S3J). Treatment of (*Rnaseh2b;p53*)$^{Nes\text{-}cre}$ cells with camptothecin (CPT), which promotes Top1cc, caused further accumulation of Top1cc compared to control cells (Figure S3J). Furthermore, the presence of Top1cc *in vivo* was confirmed by the immune complex of enzyme (ICE) assay (Katyal et al., 2014; Subramanian et al., 2001) that demonstrated an increased Top1cc accumulation in *Rnaseh2b*$^{Nes\text{-}cre}$ cerebellum (Figure 3C). In sum, our data suggest that RNASEH2 loss compromises the genomic integrity of neural cells by the accumulation of replication-associated damage, including genomic ribonucleotides, R-loops and Top1cc.

Because the accumulation of cytoplasmic DNA primes the innate immune response, we examined if damaged genomic DNA is mislocalized in the cytoplasm upon RNASEH2 loss. We stained *p53*$^{Nes\text{-}cre}$ and (*Rnaseh2b;p53)*$^{Nes\text{-}cre}$ astrocytes with single-strand DNA (ssDNA) antibody and analyzed these using flow cytometry (Hartlova et al., 2015). We observed enhanced positive staining of ssDNA in (*Rnaseh2b;p53)*$^{Nes\text{-}cre}$ cells compared to *p53*$^{Nes\text{-}cre}$ cells using flow cytometry (Figure 3D). Notably, this staining was sensitive to S1 nuclease that degrades ssDNA species, indicating specificity of ssDNA staining. Consistently, we observed enhanced ssDNA positive immunostaining of cells present in the *Rnaseh2b*$^{Nes\text{-}cre}$ cerebellum but not in the cortex region (Figure 3E & S3K). Collectively these data show that RNASEH2 deficiency-associated DNA damage stimulates cytoplasmic ssDNA accumulation, thereby priming type I interferon.

p53 deletion rescues RNASEH2-mediated cerebellar atrophy but induces medulloblastoma.

Since p53 deletion rescued cell growth of RNASEH2B-deficient cells, we investigated if it also recues neurodegeneration in *Rnaseh2b*$^{Nes\text{-}cre}$ mice. Histology and MRI analysis of (*Rnaseh2b;p53)*$^{Nes\text{-}cre}$ cerebellum showed rescue of cerebellar atrophy associated with RNASEH2 loss (Figure 4A & 4B). DNA repair-deficient mice are prone to develop medulloblastoma when p53 is co-inactivated (Dumitrache et al., 2018; Frappart et al., 2009; Lee et al., 2009; Lee and McKinnon, 2002). Accordingly, all (*Rnaseh2b;p53)*$^{Nes\text{-}cre}$ mice rapidly develop medulloblastoma (Figure S4A), with a mean survival age of 12 weeks (Figure S4B). In contrast, p53 mice did not develop any tumors until the end of the study (>6 months). Tumors showed DNA damage accumulation and were synaptophysin immunopositive (Figure S4C). To identify the molecular subtype of RNASEH2/p53-derived medulloblastoma, we performed fluorescent *in situ* hybridization analysis using PTCH1 and N-MYC probes. (*Rnaseh2b;p53)*$^{Nes\text{-}cre}$ tumors showed amplification of *Mycn* and *Ptch1* inactivation (chromosome 13 loss) (Figure S4D), suggesting that compromised genomic integrity upon RNASEH2 loss similar to other DNA repair mutants drives SHH-subtype medulloblastoma formation.

ATM suppresses neuropathology and ataxia after *Rnaseh2b* inactivation.

The ATM kinase plays a central role in maintaining genomic stability during nervous system development (McKinnon, 2012, 2017). To investigate if ATM signaling impacts the *Rnaseh2b*$^{Nes\text{-}cre}$ phenotype, we generated (*Rnaseh2b;Atm)*$^{Nes\text{-}cre}$ mice and found a striking exacerbation of the *Rnaseh2b*$^{Nes\text{-}cre}$ phenotype (Figure 4A & 4B). In contrast to WT or *Atm*$^{Nes\text{-}cre}$ cerebella (which were histologically indistinguishable), or the *Rnaseh2b*$^{Nes\text{-}cre}$ single mutant, the (*Rnaseh2b;Atm)*$^{Nes\text{-}cre}$ cerebellum was significantly smaller in size (Figure 4A) as were the mice (Figure S5A). The (*Rnaseh2b;Atm)*$^{Nes\text{-}cre}$ mice also exhibited pronounced ataxia (Figure 4C), indicating substantial neurological dysfunction. Histological and MRI analysis of (*Rnaseh2b;Atm)*$^{Nes\text{-}cre}$ brain showed a significantly smaller cerebellar volume (61% smaller than control; $p<0.0001$) (Figure 4B). However, the cortical volume was unaffected, although a modest reduction in the hippocampal volume was observed in these mice (Figure S5B & S5C). The P28 (*Rnaseh2b;Atm)*$^{Nes\text{-}cre}$ brain showed extensive disruption of cerebellar architecture with only rudimentary folia formation (Figure 4A). *P53* deletion in *Rnaseh2b*$^{Nes\text{-}cre}$ mice rescued interneurons and granule cell loss, but this did not happen after ATM inactivation (Figure 4D). Immunostaining for Pax2, an interneuron precursor marker, showed a similar result (Figure 4D), suggesting that (*Rnaseh2b;Atm)*$^{Nes\text{-}cre}$ interneuron progenitors are vulnerable early in cerebellar development. Consistently, we observed enhanced γH2AX positive cells at E15.5, P0 and P5 and TUNEL positive cells at P0 and P5 in *Rnaseh2b*$^{Nes\text{-}cre}$ and (*Rnaseh2b;Atm)*$^{Nes\text{-}cre}$ mice compared to (*Atm)*$^{Nes\text{-}cre}$ and control mice (Figure S5D, S5E & S5F), again indicating that DNA damage-mediated cell death of (*Rnaseh2b;Atm)*$^{Nes\text{-}cre}$ neural progenitors accounts for the smaller cerebellar size.

Coincident deletion of ATM and RNASEH2B in the brain also impacted other neural cell types. We found that cerebellar Purkinje cells were markedly disorganized in (*Rnaseh2b;Atm)*$^{Nes\text{-}cre}$, as determined using Calbindin and CA8 immunostaining (Figure

S5G). Oligodendrocytes were also impacted in the (*Rnaseh2b;Atm*)$^{Nes\text{-}cre}$ cerebellar white matter, with reduced oligodendrocyte numbers determined by Olig2 immunostaining and disrupted myelination judged by MBP immunostaining (Figure S5G & S5H). Collectively, our results indicate that repair of replication-induced DNA damage and the impact on neural development after RNASEH2 loss is directed by ATM.

ATM inhibits toxic NHEJ after RNASEH2 loss.

We next investigated how *Atm* deletion in *Rnaseh2b*$^{Nes\text{-}cre}$ exacerbated the neural phenotype. Our data suggest that RNASEH2 loss leads to replication stress induced DSBs. Amongst replication-associated breaks are single-ended DSBs that are preferentially repaired by homologous recombination (HR) rather than NHEJ (Magdalou et al., 2014; Zeman and Cimprich, 2014). Recent work has shown that ATM promotes repair of single-ended DSBs at the replication fork by inhibiting NHEJ to allow HR, thereby preventing aberrant chromosome fusions and cell death (Balmus et al., 2019; Britton et al., 2020; Nakamura et al., 2021). Since we observed widespread DNA damage in RNASEH2B-depleted proliferating cells, we hypothesized that ATM prevents toxic NHEJ at single-ended DSBs due to RNASEH2 loss. To test this, we generated (*Rnaseh2b;Atm; Lig4*) $^{Nes\text{-}cre}$ mice by deleting the core NHEJ factor, DNA ligase 4 (LIG4). Remarkably, *Lig4* deletion rescued the (*Rnaseh2b;Atm*)$^{Nes\text{-}cre}$ phenotype. These mice exhibited only mild ataxia with relatively normal ambulation compared to (*Rnaseh2b;Atm*)$^{Nes\text{-}cre}$ mice (Figure 4E). Histology revealed extensive rescue of the cerebellar defect in (*Rnaseh2b;Atm;Lig4*)$^{Nes\text{-}cre}$ mice (Figure 4F). Moreover, Calbindin/CA8 and MBP immunostaining indicated partial rescue of Purkinje neuron organization and oligodendrocytes in (*Rnaseh2b;Atm;Lig4*)$^{Nes\text{-}cre}$ compared to (*Rnaseh2b;Atm*)$^{Nes\text{-}cre}$ mice (Figure 4G). Thus, suppression of toxic NHEJ by ATM mitigates the impact of RNASEH2B loss. NHEJ pathway avoidance likely promotes survival of RNASEH2B-ATM deficient neural cells via repair of DSBs by HR.

We also reasoned that misrepaired DSBs in RNASEH2B-ATM deleted cells by NHEJ lead to genomic instability and those cells undergo p53-mediated cell death. Therefore, we generated (*Rnaseh2b;Atm;p53*)$^{Nes\text{-}cre}$ mice and found that the deletion of p53 rescued ataxia and cerebellar atrophy of (*Rnaseh2b;Atm*)$^{Nes\text{-}cre}$ mice (Figure 4E, 4F & 4G). This suggests genome instability due to aberrant repair of DNA by NHEJ in the cerebellum activates p53-dependent apoptosis in (*Rnaseh2b;Atm*)$^{Nes\text{-}cre}$ mice (Figure S5).

ATM restrains neuroinflammation and type I interferon in *Rnaseh2b*$^{Nes\text{-}cre}$ mice.

Given the surprising severity of (*Rnaseh2b;Atm*)$^{Nes\text{-}cre}$ phenotype, we asked how transcriptional programs influenced by RNASEH2B might be affected, particularly those associated with inflammation. Differential gene expression analysis using Poly A+ RNA-seq revealed ~2,000 differentially expressed genes in (*Rnaseh2b;Atm*)$^{Nes\text{-}cre}$ compared to control cerebellum ($Log_2FC > 1 < -1$, FDR <0.05) (Figure 5A & Suppl. Data Table 2). Intriguingly, immune-related pathways including, the "*role of pattern recognition receptors in recognition of bacteria and viruses*" pathway were identified amongst the top significantly enriched pathway by IPA (Figure 5B & & S6A). Next, we investigated if there are any upstream regulators that may be responsible for the gene expression changes observed in our mRNA dataset using IPA upstream regulator analysis. Various immune-related

molecules such as, STAT1, TGF and IFNG were identified as the top 10 upstream regulators (Figure S6B). To further test if ATM loss in RNASEH2B-deficient cerebellum enhances the expression of type I interferon response, we performed GSEA analysis. Notably, we observed a significant enrichment of the type I interferon-alpha response pathway genes in (*Rnaseh2b;Atm*)$^{Nes\text{-}cre}$ cerebellum in comparison to control or (*Atm*)$^{Nes\text{-}cre}$ cerebellum (Figure 5C, 5D & Table S1). ATM deficiency has also been linked with the activation of the innate immune response (Hartlova et al., 2015; Quek et al., 2017; Song et al., 2019). However, we did not observe any significant accumulation of type I interferon alpha response pathway genes in *Atm*$^{Nes\text{-}cre}$ cerebellum, while we observed enrichment of type I interferon alpha response pathway genes in *Rnaseh2b*$^{Nes\text{-}cre}$ cerebellum compared to control (Figure 5D, S6C & Table S1). qRT-PCR analysis further confirmed a significant increase in transcript levels of *Irf7*, *Igtp* and *Ifit1* interferon-stimulated genes in (*Rnaseh2b;Atm*)$^{Nes\text{-}cre}$ (Figure 5E). We also observed enhanced micronuclei formation in *Rnaseh2b*$^{Nes\text{-}cre}$ and (*Rnaseh2b;Atm*)$^{Nes\text{-}cre}$ astrocytes compared to control and *Atm*$^{Nes\text{-}cre}$ cells (Figure 5F).

We next investigated if the (*Rnaseh2b;Atm*)$^{Nes\text{-}cre}$ mRNA-seq data was similar to publicly available disease datasets using the IPA analysis match feature. Strikingly, one of the top matches was “viral infectious disease mouse fetal brain; Zika virus” (GSE89069.GPL19057; overall Z score 44.98) (Figure S6D). Other matched datasets were: (1) Amyotrophic Lateral Sclerosis (ALS; mouse cervical spinal cord; GSE112629.GPL19057; overall Z score 45.67), (2) Viral infectious disease (mouse spleen; GSE146074.GPL24247; overall Z score 44.81), (3) Frontotemporal lobar degeneration (FTLD; mouse brain stem; GSE90693.GPL13112; overall Z score 44.63 and (4) Neuropathic Gaucher disease (nGD; mouse thalamus; GSE46866.GPL6246; overall Z score 44.34). Comparison analyses revealed that the top overlapping pathways were immune-signaling-related pathways including, “*neuroinflammation signaling pathway*” and the most highly enriched upstream regulators include IFNG and IFN-α, among other inflammation-related factors (Figure S6D & S6E). This data further corroborate our other findings that inhibiting ATM signaling in the *Rnaseh2b*$^{Nes\text{-}cre}$ brain leads to inflammatory gene expression changes associated with human disease.

Because we observed DNA damage in these mice during early neurogenesis, we next asked if type I IFN signaling is activated during postnatal cerebellar development. To test this, we analyzed gene expression in *Rnaseh2b*$^{Nes\text{-}cre}$, (*Rnaseh2b; Atm*)$^{Nes\text{-}cre}$, (*Rnaseh2b;p53*)$^{Nes\text{-}cre}$, *p53* $^{Nes\text{-}cre}$, *Atm* $^{Nes\text{-}cre}$ and control P5 cerebellum using RNA-seq. There were ~1,200 genes found to be differentially regulated in the(*Rnaseh2b;Atm*)$^{Nes\text{-}cre}$ cerebellum compared to control (Log_2FC >1, <−1, FDR <0.05; Table S2). Analysis of differentially expressed genes using the IPA graphical summary feature identified immune-related pathways as one of top overrepresented pathways, consistent with P28 data (Figure S7A). However, only ~30 genes were found to be differentially regulated in the *Rnaseh2b*$^{Nes\text{-}cre}$ in comparison to control (Table S2). Consistent with DNA damage-dependent signaling in the *Rnaseh2b*$^{Nes\text{-}cre}$ at P5, “*p53 signaling”* and *“apoptosis signaling*” were identified as one of the top 10 enriched canonical pathways (Figure S7B). We next compared gene expression of various genotypes using IPA. Notably, “*neuroinflammation signaling pathway”* and “*Interferon-α*” (the top predicted upstream cytokine) were found to be significantly enriched in the (*Rnaseh2b;Atm*)$^{Nes\text{-}cre}$, (*Rnaseh2b;p53*)$^{Nes\text{-}cre}$

and *Rnaseh2b*$^{Nes\text{-}cre}$ cerebellum (Figure S7C & S7D). (*Rnaseh2b;Atm)*$^{Nes\text{-}cre}$ and (*Rnaseh2b;p53)*$^{Nes\text{-}cre}$ cerebellum show higher enrichment of inflammation signaling in comparison to *Rnaseh2b*$^{Nes\text{-}cre}$. In contrast, *p53*$^{Nes\text{-}cre}$ and *Atm*$^{Nes\text{-}cre}$ cerebellar gene expression did not show significant enrichment of inflammation-related gene signatures (Figure S7C & S7D). GSEA analyses of type I interferon pathway further corroborated these data (Figure S7E & Table S1).

To further test if additional inflammation pathways are upregulated in the absence of RNASEH2, we performed GSEA analysis for NF- κB pathway. Interestingly, we observed activation of Hallmark TNF signaling via NF- κB in the *Rnaseh2b*$^{Nes\text{-}cre}$ and (*Rnaseh2b;Atm)*$^{Nes\text{-}cre}$ cerebellar tissues (P28 and P5) compared to (*Atm)*$^{Nes\text{-}cre}$ and control (Figure S7F & Suppl. Data Table 1). Notably, (*Rnaseh2b;p53)*$^{Nes\text{-}cre}$ cerebellar P5 tissue did not show enrichment of TNF signaling via NF- κB while it had enhanced type I interferon signaling (Figure S7F & Table S1), indicating that RNASEH2-dependent cell death might account for activation of TNF signaling via NF-κB but not the type I interferon signaling.

We next investigated if neuroinflammation is also enhanced in (*Rnaseh2b;Atm)*$^{Nes\text{-}cre}$ mice. To test this, we employed a mouse inflammatory cytokine array. Secretion of various inflammatory factors such as CCL9, CXCL1 and CCL2 was enhanced in the *Rnaseh2b*$^{Nes\text{-}cre}$ and more so in the (*Rnaseh2b;Atm)*$^{Nes\text{-}cre}$ astrocytes compared to control and ATM -deficient cells (Figure 5G). Additionally, GFAP and Iba1 immunoreactivity was substantial in (*Rnaseh2b;Atm)*$^{Nes\text{-}cre}$ and *Rnaseh2b*$^{Nes\text{-}cre}$ P28 brains compared to control brains (Figure 6A & 6B). The Iba1 positive microglia in mutant brains were less ramified with shorter projections and some exhibited amoeboid morphology, indicating a reactive microglial state (Figure 6B). Thus, these data suggest ATM signaling is crucial in limiting neuroinflammation in the context of RNASEH2B deficiency.

Microglia exhibit distinct reactive states in response to neurodegeneration in *Rnaseh2b*$^{Nes\text{-}cre}$ and (*Rnaseh2b;Atm)*$^{Nes\text{-}cre}$ mice.

Microglia are specialized tissue-resident macrophages in the brain that respond to any perturbation in the brain by undergoing rapid multistage transformation resulting in an alteration in shape, gene expression and functional properties (Nayak et al., 2014). A recent study using single-cell RNA-seq identified distinct and disease stage-specific microglia gene expression signatures in a neurodegeneration model with Alzheimer's disease-like phenotype with an 'early-response' vs 'late-response' microglia state (Mathys et al., 2017). To identify if there are distinct microglia phenotypes over the course of neurodegeneration in *Rnaseh2b*$^{Nes\text{-}cre}$ and (*Rnaseh2b;Atm)*$^{Nes\text{-}cre}$, we compared our transcriptomics data with the Mathys et. al., data set. Intriguingly, GSEA showed an enrichment of microglia 'early-response' gene set (represented by cluster 3 and cluster 7) in the *Rnaseh2b*$^{Nes\text{-}cre}$ at P5 and P28 stage of cerebellum development (Figure 6C & Table S1). The 'late-response' microglia (cluster 6) gene set showed enrichment in the 9-week-old samples, suggesting that microglia phenotypic state changes as the neurodegeneration progresses in *Rnaseh2b*$^{Nes\text{-}cre}$ mouse (Figure 6C & Table S1). In contrast, we observed significant enrichment (FDR <0.05) of the 'late-response microglia' (cluster 6) gene set at P5 and P28 in the (*Rnaseh2b;Atm)*$^{Nes\text{-}cre}$ cerebellum in comparison to control or *Atm*$^{Nes\text{-}cre}$, but no positive enrichment of either

the ‘early-response’ or ‘late-response’ microglia gene cluster was observed in the ATM-deficient tissue (Figure 6C & Table S1). This data suggests that microglia may acquire distinct reactive states during cerebellar development to counter the extensive neuronal cell death caused due to combined deficiency of RNASEH2 and ATM.

To further uncover the basis of microglia heterogeneity, we investigated if there are any transcription factors that drive the reactive microglia phenotype. We found enrichment of genes that are targets of interferon regulatory factor 8 (IRF8) transcription factor in *Rnaseh2b*$^{Nes\text{-}cre}$ and (*Rnaseh2b;Atm*)$^{Nes\text{-}cre}$ but not in *Atm*$^{Nes\text{-}cre}$ cerebellum (Figure 6C & Suppl. Data Table 1). IRF8 is a key regulator that is required for maturation of microglia and is also associated with the activation of microglia into a reactive phenotype (Kierdorf et al., 2013; Masuda et al., 2012; Zhou et al., 2019). We observed that a majority of known IRF8 consensus targets were associated with ‘late-response’ microglia (~29 genes overlap), while minimal overlap was seen with ‘early-response’ microglia gene cluster 3 and cluster 7 (Figure 6C). We did not observe significant enrichment of genes that are target of interferon regulatory factor 1 (IRF1; a transcription factor that plays a role in both homeostatic and reactive microglia states (Gao et al., 2019; Masuda et al., 2015) in the *Rnaseh2b*$^{Nes\text{-}cre}$ and (*Rnaseh2b;Atm*)$^{Nes\text{-}cre}$ cerebellum, thus suggesting specific response to IRF8 (Figure 6C & Table S1). Correlation analysis between *Rnaseh2b*$^{Nes\text{-}cre}$ and (*Rnaseh2b;Atm*)$^{Nes\text{-}cre}$ suggested that although IRF8 target genes are enriched in *Rnaseh2b*$^{Nes\text{-}cre}$, they are further affected in (*Rnaseh2b; Atm*)$^{Nes\text{-}cre}$ as shown by the increase in positive slope (Figure 6D). But IRF1 gene sets show a similar trend to the general pattern observed by all genes when compared between *Rnaseh2b*$^{Nes\text{-}cre}$ and (*Rnaseh2b;Atm*)$^{Nes\text{-}cre}$ (Figure 6D). Our data suggests that IRF8 is one of the transcription factors that drive the microglia reactive phenotype in response to neurodegeneration in *Rnaseh2b*$^{Nes\text{-}cre}$ and (*Rnaseh2b;Atm*)$^{Nes\text{-}cre}$ mice.

DNA damage signaling independent of type I IFN signaling drives neurodegeneration in *Rnaseh2b*$^{Nes\text{-}cre}$ mice.

Type I IFN signaling is essential for antiviral immunity, but its deregulation can be noxious to cells, leading to neurodegeneration in mice (Akwa et al., 1998; Campbell et al., 1999). Since type I IFN induction is proposed to be responsible for AGS pathogenesis (Crow, 2011; Lee-Kirsch, 2017), we investigated if type I IFN signaling has a key role in *Rnaseh2b*$^{Nes\text{-}cre}$ or (*Rnaseh2b;Atm*)$^{Nes\text{-}cre}$ neuropathology. To examine this, we deleted cGAS, a key factor required for STING mediated type I IFN activation (Hopfner and Hornung, 2020; Motwani et al., 2019). (*Rnaseh2b;Atm*)$^{Nes\text{-}cre}$;*cGAS*$^{-/-}$ mice developed ataxia and appeared similar to (*Rnaseh2b;Atm*)$^{Nes\text{-}cre}$ mice. Histology and MRI analysis indicated that although cGAS deletion slightly rescues cerebellar size of *Rnaseh2b*$^{Nes\text{-}cre}$ this was not the case for the (*Rnaseh2b; Atm*)$^{Nes\text{-}cre}$ cerebella (Figure 7A & 7B). Moreover, enhanced GFAP immunoreactivity was still apparent after cGAS deletion in *Rnaseh2b*$^{Nes\text{-}cre}$ and (*Rnaseh2b;Atm*)$^{Nes\text{-}cre}$ cerebellum (Figure 7C). In contrast, cGAS deletion effectively rescued the constitutive type I IFN signaling in *Rnaseh2b*$^{Nes\text{-}cre}$ and (*Rnaseh2b;Atm*)$^{Nes\text{-}cre}$ astrocytes, as shown by qPCR analysis of ISG genes *Ifit1, Ifit3 and Irf7* (Figure 7D). To further confirm the role of cGAS signaling, we challenged cells with poly(dA:dT) (a synthetic dsDNA analog) and poly(I:C) antigens (a synthetic dsRNA analog). We

observed heightened IFN signaling in *Rnaseh2b*$^{Nes\text{-}cre}$ astrocytes when cells were stimulated with either poly(dA:dT) or poly(I:C) antigen compared to rest of group, indicating that RNASEH2-depleted cells are already primed for type I IFN induction. Importantly, cGAS deletion significantly rescued the poly (dA:dT), but not the poly(I:C), induced type I IFN response in RNASEH2-deficient cells (Figure 7E & 7F), confirming that RNASEH2 disruption leads to activation of a DNA sensing pathway. Importantly, p53 deletion in (*Rnaseh2b*;*Atm*)$^{Nes\text{-}cre}$ cells resulted in a heightened type I IFN signaling (Figure 7G), suggesting that enhanced DNA damage sensitizes cells to mount an exaggerated type I IFN response.

Recently, cGAS signaling has been shown to play a role in maintenance of the senescence phenotype (Gluck et al., 2017; Yang et al., 2017). RNASEH2B loss results in senescence in cells, but this phenotype was not rescued in *Rnaseh2b*$^{Nes\text{-}cre}$;cGAS$^{-/-}$ astrocytes (Figure 7H). qPCR analysis for known senescence markers, p21 and p16 validated that *Rnaseh2b*$^{Nes\text{-}cre}$;*cGAS*$^{-/-}$ cells undergo senescence similar to *Rnaseh2b*$^{Nes\text{-}cre}$ cells, suggesting that cGAS depletion does not revert the senescent phenotype of *Rnaseh2b*$^{Nes\text{-}cre}$ cells (Figure 7H). Despite activated type I IFN signaling in the (*Rnaseh2b*;*Atm*)$^{Nes\text{-}cre}$ brain, our data collectively indicate that neuropathology is mainly driven by DNA damage.

Discussion:

AGS is considered an autoinflammatory disorder that is characterized by severe brain dysfunction, although the underlying pathogenic lesion responsible for neuropathology remains unclear. In this study, we show that after RNASEH2B inactivation, genome instability rather than type I IFN signaling is a key driver of AGS neuropathology. Ribonucleotide incorporation is one of the most frequent types of DNA damage encountered by cells (Kellner and Luke, 2020; McElhinny et al., 2010; Reijns et al., 2012). DNA damage in the *Rnaseh2b*$^{Nes\text{-}cre}$ brain was prevalent in the proliferating neural progenitor cells, suggesting that embedded ribonucleotides compromises genomic integrity of neuroprogenitors, leading to p53-dependent cell death. Interestingly, studies have reported that AGS patients, particularly those harboring *RNASEH2B* mutations, show neurological decline in the first year of life and then stabilize, despite showing enhanced type I interferon signaling, raising the question of disease etiology (Crow et al., 2015; Livingston and Crow, 2016; Rice et al., 2007). Since, RNASEH2 deficiency in mice impacted embryonic and postnatal neurogenesis, our data may explain why progression of the disease is muted in the mature nervous system.

Consistently, we found RNASEH2 deletion in proliferative or immature neural cells resulted in accumulation of γH2AX foci and micronuclei formation. During replication, frequent single-ended DSBs occur due to collision of a replication fork with various types of DNA damage (Cortez, 2019). Since these breaks lack another DNA end to be ligated by NHEJ pathway, they are preferentially repaired by HR (Bouwman and Crosetto, 2018; Magdalou et al., 2014). The ATM kinase can play a key role in regulating DSB repair by promoting efficient DSB resection and suppression of the NHEJ pathway (Balmus et al., 2019; Britton et al., 2020; Nakamura et al., 2021). Our data show that ATM is activated after RNASEH2 loss in response to DNA breaks and its deletion exacerbates the

cerebellar atrophy and the neuroinflammation in *Rnaseh2b*$^{Nes\text{-}cre}$ mice. This exacerbation is due to misrepair from toxic NHEJ, leading to p53-dependent neuronal cell death. This is corroborated by Lig4 deletion to inhibit NHEJ, which rescues the neural pathology and ataxia of (*Rnaseh2b;Atm*)$^{Nes\text{-}cre}$ mice, suggesting ATM acts as a surveillance factor to counteract the deleterious end-joining at single-ended DSBs resulting from RNASEH2 deficiency.

Recognition of self-DNA by the cGAS-STING signaling axis has emerged as one of the key pathways connecting DNA damage and innate immune activation (Hopfner and Hornung, 2020; Li and Chen, 2018). In agreement with this, we find RNASEH2B-depleted neural cells show accumulation of cytoplasmic DNA. Additionally, cGAS signaling is activated in response to RNASEH2-mediated neural DNA damage showing robust immune activation during early cerebellar development. Notably, the (*Rnaseh2b;p53*)$^{Nes\text{-}cre}$ and (*Rnaseh2b;Atm*)$^{Nes\text{-}cre}$ mice show substantially augmented expression of interferon-stimulated genes compared to *Rnaseh2b*$^{Nes\text{-}cre}$. Although p53 inactivation rescued cell death, our data indicate that (*Rnaseh2b;p53*)$^{Nes\text{-}cre}$ cells accumulate more DNA damage, as evidenced by increased micronuclei and multinucleation defects. Treatment of RNASEH2-deficient fibroblasts with UV also enhanced the type I IFN production compared to untreated cells (Gunther et al., 2015), substantiating our studies that increased DNA damage activates a heightened immune response. Thus, AGS patients who carry additional mutations or variant alleles in DNA repair genes might have a greater risk for developing autoimmunity.

Microglia are innate immune cells of the brain that play a key role in maintaining brain homeostasis by clearing dying neurons (Colonna and Butovsky, 2017). A caveat of our mouse model is that RNASEH2B and ATM are not depleted in microglia by Nestin-cre, as these cells derive from the yolk sack (Ginhoux et al., 2010). Despite this, we observed a striking activation of microglia in the (*Rnaseh2b;Atm*)$^{Nes\text{-}cre}$ brain, indicating that these cells are activated in a non-cell autonomous manner. This further indicates that neural DNA damage can initiate a vicious cycle where microglia respond to perturbed neural homeostasis and their activation results in an inflammatory response. Since AGS-associated *RNASEH2B* mutations also affect microglia, it would be interesting to assess the effect of either further or specific *Atm* and *Rnaseh2b* deletion in microglia.

A key finding from our study is that type I IFN signaling is not the primary mediator of neural dysfunction in *Rnaseh2b*$^{Nes\text{-}cre}$ mice. However, we do note that cGAS inactivation mildly improves the *Rnaseh2b*$^{Nes\text{-}cre}$ phenotype, supporting a contributing role of IFN signaling to neurodegeneration. Type I IFNs are potent immunomodulatory cytokines that protects host against viral and intracellular pathogens (Boxx and Cheng, 2016; McNab et al., 2015; Mesev et al., 2019). However, inappropriate expression of type I IFNs is associated with AGS pathology (Crow, 2011; Lee-Kirsch, 2017). Overexpression of IFN-α in a transgenic mouse model exhibits neurodegeneration and white matter abnormalities (Akwa et al., 1998; Campbell et al., 1999; Crow and Manel, 2015; Lee-Kirsch, 2017). Similarly, *in utero* HIV infection mimics phenotypes of AGS (Crow and Manel, 2015; DeCarli et al., 1993; Kauffman et al., 1992). These data point to a causal link between type I IFNs and AGS, but if chronic overactivation of type I IFNs is truly pathogenic is has not yet been validated. Importantly, AGS individuals with RNASEH2B mutations show

variable interferon expression as some exhibit either a negative interferon signature despite presenting with other clinical phenotypes or have lower median interferon scores compared to AGS resulting from mutations in other genes (Garau et al., 2019; Rice et al., 2013).

Our data supports chronic DNA damage as the key driver of neurodegeneration in AGS after RNASEH2 inactivation. This conclusion is reinforced by cGAS depletion restoring appropriate type I IFN signaling but not preventing neurodegeneration. In contrast, inactivation of p53-mediated DNA damage signaling protected mice from cerebellar atrophy, despite heightened IFN signaling. Neurodegeneration was therefore dependent upon susceptibility of neural cell progenitors to DNA damage-induced cell death. Accordingly, while aberrant expression of type I IFN is toxic to neural cells, it might not be the primary cause of neurodegeneration seen in AGS. Notably, TREX1 and SAMHD1-deficeint fibroblasts-derived from AGS patient show impaired proliferation and chronic DNA damage (Kretschmer et al., 2015; Park et al., 2021; Yang et al., 2007), underscoring the likelihood that activation of DNA damage signaling contributes critically to neuropathology in AGS. While our findings establish the importance of RNASEH2 during neurogenesis, critically they provide key insight for the neurological phenotypes associated with AGS to guide future studies on the pathogenesis of this debilitating disease.

STAR Methods:

Resource Availability

Lead Contact—Further information and requests for reagents may be directed to the lead contact, Peter J. McKinnon (peter.mckinnon@stjude.org).

Materials Availability—The materials generated in this paper are available from the lead contact upon request, in some cases after completion of a standard MTA.

Data and Code Availability—RNA Seq data has been deposited at GEO (https://www.ncbi.nlm.nih.gov/geo/, Accession #GSE181159) and is publicly available, or can be obtained from the lead contact upon request. The data sets used in this study are from (Rosenberg et al., 2018), (Hanzelmann et al., 2013; McKenzie et al., 2018) and (Mathys et al., 2017) and also ENCODE and ChEA Consensus TFs from ChIP-X library in Enrichr. No new software or code was generated in this study.

Experimental model and subject details

Mice: *Rnaseh2b*$^{tm1a(EUCOMM)Wtsi}$ embryos were obtained from EUCOMM/Welcome Trust Sanger Institute [Cat #05078] and reconstituted in the cryopreservation core at SJCRH. The *Rnaseh2b*^{tm1a} allele is designed to include a cassette composed of *FRT* flanked LacZ/neomycin sequence followed by a *LoxP* site. An additional *LoxP* site is located downstream of critical exon 5, which generates a prematurely truncated *Rnaseh2b* transcript. *Rnaseh2b* mice were initially crossed with Flp recombinase mice to remove LacZ. To generate neural-wide *Rnaseh2b* deletion, the *Rnaseh2b*^{tm1a} mice were then crossed with *Nestin-cre* mice (B6.Cg-Tg(Nes-cre)1Kln/J, JAX #003771). Genotypes were determined by PCR as recommended by the vendor (see Table S3). *cGAS*$^{-/-}$ mice were obtained from the Jackson

Laboratory (B6(C)-*Cgas* $^{tm1d(EUCOMM)Hmgu}$/J; Stock No: 026554). Conditional *Atm, p53, Lig4* and *Xrcc1* alleles have been described previously (Frappart et al., 2009; Jonkers et al., 2001; Lee et al., 2009; Lee et al., 2012). Experiments were performed with mice of either sex, although whenever possible littermate mice were sex matched. We did not observe any influence of sex on the outcome of experiments. The age of mice used for experiments is specified in the text and figures. Mice were housed at AAALAC-accredited facility. All animal procedures were approved by the SJCRH animal care and use committee.

Primary cell culture

Isolation of neural stem cells, astrocytes and treatments: Neural stem cells were derived from E15.5 embryos. Embryonic brains were collected in cold PBS+2% glucose. After removing meninges, brain hemispheres were dissociated by mechanical trituration (20 strokes with a fire polished Pasteur pipette). Cells were resuspended in NeuroCult NSC basal media (STEMCELL Technologies) supplemented with 20ng/ml recombinant human EGF and cultured in a T25 flask. Cells were maintained in a humidified incubator at 37°C and 5% CO_2.

Primary astrocytes were isolated from P2-P3 mouse pups of either sex. Mouse cortices were dissected from brain and meninges were removed under a dissecting microscope. Cortices were dissociated by passing through 5-ml pipets. Cells were resuspended in DMEM/F12 (1:1) media (Gibco) supplemented with 10% fetal bovine serum (Gibco), 1x glutamax,100mg/ml streptomycin, 100U/ml penicillin and 20ng/ml epidermal growth factor. Primary astrocytes were cultured in Primaria T-25 flasks in a humidified incubator at 37°C and 5% CO_2. After four days, media was changed, and cells were allowed to grow for an additional one or two days before cells were further passaged. Astrocyte culture purity was assessed by GFAP immunostaining. Astrocytes were transfected with either 1.5 μg/ml poly(I:C) (Invivogen) or 1.5μg/ml poly(dA:dT) (Invivogen) reagent using Xfect transfection reagent (Takara Bio) following manufacturer's instructions. Camptothecin treatment was 10μM for 1h. Experiments were performed in triplicate.

Method details

Histology and Immunohistochemistry: Brain tissues were collected at the indicated ages after transcardial perfusion with 4% buffered paraformaldehyde (PFA), while embryos were drop fixed in 4% buffered PFA. After overnight fixation at 4°C, brains were cryoprotected in 25% sucrose solution (w/v) in PBS. Tissues were embedded in tissue freezing media (OCT: Electron Microscopy Sciences) and cryo-sectioned at 10μm using a HM 525 NX cryostat (Thermo Fisher Scientific). Hematoxylin & Eosin staining was performed according to standard procedures. For immunostaining, frozen sections were washed in PBS and subjected to antigen retrieval (HistoVT One) following the manufacturer's recommendation. Samples were blocked for 1h with blocking buffer (5% normal donkey serum/1% BSA/0.3% Triton X 100 in PBS). Sections were incubated with diluted primary antibodies in blocking buffer overnight with gentle agitation. The following primary antibodies were used; Calbindin (1:500, Sigma-Aldrich, C9848), CA8 (1:500, Novus Biologicals, NB100–74382), GFAP (1:500, Sigma-Aldrich, G3893), γH2AX (Ser-139, 1:500, Cell Signaling Technology, 2577), Iba1 (1:500, Novus

Biologicals, NB100–1028), NeuN (1:500, Millipore, MAB377), Parvalbumin (1:500, Millipore, MAB1572),Olig2 (1:500, Millipore, AB9610), Phospho KAP1-S824 (1:500, Bethyl Laboratories, A300–767A), 53BP1 (1:500, Bethyl Laboratories, A300–272A), PCNA (PC-10)(1:500, Santa Cruz Biotechnology, Sc56), Pax2 (1:500, Invitrogen, 71–6000), CNPase (1:400, Sigma-Aldrich, C5922), MBP (1:500, Abcam, ab40390). After three washes in PBS, sections were incubated for 1h with the appropriate Alexa Fluor 488 and 555-conjugated secondary antibodies. Tissue sections were mounted using ProLong Gold antifade with DAPI mounting media (Invitrogen). Cell death was assessed by the TUNEL assay using ApopTag-fluorescein in situ apoptosis detection kit (Millipore) according to the manufacturer's instructions. Sections were mounted using Vectashield antifade with propidium iodide mounting media (Vector Laboratories). All experiments were performed at least in triplicate.

ssDNA immunostaining: Frozen sections were processed for antigen retrieval followed by incubation with 3% H_2O_2/methanol for 10 min to block endogenous peroxidase activity. After three washes with PBS, sections were blocked for 1h with blocking buffer (5% normal donkey serum/1% BSA/0.3% Triton X 100 in PBS) and then incubated with ssDNA antibody overnight (1:20 dilution, Millipore, MAB3299). Following washes with PBS, sections were incubated with HRP-conjugated secondary antibody (1:200 dilution) for 90 min at RT. Immunodetection was performed using a DAB (3,3'diaminobenzidine) peroxidase substrate kit (Vector Laboratories) according to the manufacturer's recommendation. Sections were dehydrated and mounted with DPX (Electron Microscopy Sciences). For S1 nuclease treatment, after antigen retrieval step, samples were washed with PBS followed by two washes with distilled water. Sections were incubated with S1 nuclease enzyme (1000 units/ml; Invitrogen) for 4h at 37°C. Slides were washed four times with PBS and then immunostained with ssDNA antibody. Experiments were performed in triplicate. Experiments were performed in triplicate.

Immunocytochemistry and SA-β-galactosidase assay: Primary astrocytes were plated on gelatin coated round glass coverslips in a 24 well plate. Cells were fixed with 4% paraformaldehyde in PBS for 15 min at room temperature (RT). Cells were permeabilized with 0.5% Triton X-100/PBS for 5 min and blocked with 10% normal donkey serum/PBS blocking buffer for 1h. Cells were incubated with the respective primary antibodies at 4°C overnight followed by Alexa Flour 488/555-conjugated secondary antibodies. Coverslips were mounted on glass slides using Prolong Gold antifade (Thermo Fisher Scientific) with DAPI mounting media. For Top1cc immunofluorescence, cells were permeabilized with 0.25% Triton X-100/PBS for 15 min followed by treatment with 1% SDS/PBS for 5 min. Cells were washed four times with PBS and the remining immunostaining protocol was followed with Top1cc antibody (1:100, Millipore, MABE 1084). To detect RNA:DNA hybrids, cells were fixed with precooled methanol-acetic acid (1:1) for 20 min at −20°C. Cells were treated with 0.5% Triton X-100/PBS for 5 min followed by S9.6 immunostaining (1:500, Kerafast, ENH001). To measure senescence, SA-β-Gal staining (Cell Signaling Technology) was performed according to the manufacturer's instructions. All experiments were performed at least in triplicate.

RNA isolation and quantitative PCR: Total RNA was isolated using TRIzol (Invitrogen) following the manufacturer's instructions. cDNA synthesis was performed using SuperScript III first-strand synthesis kit (Invitrogen) or SuperScript IV VILO master mix with ezDNAse enzyme kit (Invitrogen). To determine relative mRNA levels, qPCR was performed using Power SYBR green PCR master mix (Applied Biosystems). A 20μl reaction was set up with 1μl of diluted cDNA, 0.4μl of 10μM primer pair and 10μl master mix. SYBR green incorporation was measured on an Applied Biosystems 7500 Real-Time PCR Machine (Applied Biosystems) with the following protocol: 50°C (2 min), 95°C (10 min) followed by 40 cycles of 95°C (15 s) and 60°C (1 min). GAPDH was used to normalize gene expression. Relative mRNA expression was calculated using the $2^{-\Delta\Delta CT}$ method (Schmittgen and Livak, 2008). All primer sequences are listed in Supplementary Table 3.

MRI: MRI was performed using a Bruker ClinScan 7T MRI system (Bruker BioSpin MRI GmbH, Ettlingen, Germany) equipped with a 12S gradient coil. A receive-only mouse brain surface coil was placed over the mouse head, and the mouse was placed inside a 72mm transmit-receive volume coil. Animals were anesthetized and maintained with 1.5–2% isoflurane during the experiments. After the localizer, a T2-weighted turbo spin echo sequence was performed in the coronal (TR/TE=2380/42ms, matrix size=256 × 256, slice thickness=0.5mm, number of slices=15) and axial (TR/TE=2500/41ms, matrix size=256 × 192, slice thickness=0.5mm, number of slices=32) orientations. Next, a diffusion tensor imaging scan using a single-shot EPI technique was done (TR/TE=3500/30ms, matrix size=128 × 100, slice thickness=0.5mm, number of slices=8, b-values=0, 1000s/mm^2, directions=12, number of averages=10). After the scans, the volumes of the cerebral cortex, cerebellum, hippocampus, and whole brain were measured by drawing regions of interest (ROI) using OsiriX (OsiriX Imaging Software, Geneva, Switzerland). Analysis of the diffusion was done in the Functional Magnetic Resonance Imaging of the Brain Software Library (FSL), which was used to produce a fractional anisotropy (FA) map of the brain. The resulting map was used to calculate the average FA value of the corpus callosum. N=3–5 mice used per individual genotype.

Immunodetection of Top1-DNA covalent complexes (ICE assay): Top1-DNA covalent complexes were isolated using an ICE assay as previously described (Katyal et al., 2014), with minor modification. Mouse brains were collected in ice-cold PBS, 2%FBS pH 7.0 for initial cleaning and dissection of the tissues. Tissues were lysed in 1% sarkosyl (w/v) with dounce homogenization for minimum 30 strokes and transfer to a prechilled 14ml BD falcon round bottom tube. The lysates were sheared using 3mL syringe with 25G$^{5/8}$ needle (10 strokes). These lysates were gently layered onto a CsCl cushion (density gradient of 0.84–1.72g/ml) in 5ml OptiSeal tubes and centrifuged in a NVT90 rotor at 42,000rpm for 20h at 25°C (Beckman Coulter). The pellets of Top1cc were washed with 70% ethanol, air dried and resuspended in 500ul 1x TE buffer. Top1cc samples were diluted with 25mM sodium phosphate buffer (pH 6.5) and applied to a nitrocellulose membrane using a slot-blot vacuum manifold (Bio-Rad). Membranes equilibrated with 25mM NaP (pH 6.5) and UV-crosslinked (1.2×10^5 J/cm^2), blocked in 5% milk/TBST and incubated overnight at 4°C with a polyclonal antibody to Top1(1:1,000, Bethyl Laboratories, 302–590A). Blots were

washed 3 times with PBST and goat anti-rabbit HRP secondary antibody (1:5,000) was added for 1hr at RT. The chemiluminescent signals were measured using a LI-COR Odyssey Fc (LI-COR). To assess DNA loading, the membrane was stained with SYBR Gold staining (Thermo Fisher Scientific) for 20 mins at RT and images were acquired using LI-COR Odyssey Fc imaging system (LI-COR).

Flow cytometry: Cells were resuspended in 1 ml of cold PBS and then 6 ml of methanol precooled to −20°C was slowly added. Cells were fixed overnight at 20°C. After two washes with PBS, cells were blocked with 5% donkey serum/PBS for 15 min. Samples were incubated with ssDNA antibody (Millipore, 1:10 dilution) for 1h at RT. Cells were washed and incubated with AlexaFlour-488 conjugated-secondary antibody (1:100 dilution). For S1 nuclease treatment, cells were incubated with S1 nuclease enzyme (Invitrogen, 400 U/ml) for 90 min at 37°C after fixation, and then immunostained. Data was collected on a BD Biosciences Fortessa and analyzed using BD Biosciences DiVa software. Single cells selected by first gating on light scatter followed by selection of single cells using side scatter width vs forward scatter area were interrogated for Alexa 488 fluorescence. Results were displayed as histograms of Alexa 488 fluorescence.

Mouse inflammation array: Astrocytes were resuspended at a density of 500,000 cells/ml and seeded in a 6 well dish, and cell culture media was collected the following day. The supernatant was assayed using the mouse inflammation antibody array (Ray Biotech) according to the manufacturer's instruction. Briefly, antibody coated membranes were blocked with blocking buffer for 1h at RT. Supernatants were incubated with the antibody arrays overnight at 4°C. Membranes were washed with wash buffer provided with the kit and then incubated with diluted biotin-conjugated secondary antibody for 2h at RT. Following washing, diluted HRP-streptavidin solution was incubated with the membranes for 2h at RT. Membranes were washed extensively with wash buffer provided with the kit and immunocomplexes were detected using detection buffer. Images were captured on LI-COR Odyssey Fc imaging system (LI-COR).

Alkaline gel electrophoresis assay: Genomic DNA was purified from cells using QIAmp DNA mini kit (Qiagen). 3μg of DNA in AE buffer (Qiagen Kit) was either kept on ice or treated with 0.3M NaOH (final concentration) for 2h at 55°C as described previously (Reijns et al., 2012). At the end of reaction, DNA was suspended in 6x alkali loading dye (6mM EDTA, 300mM NaOH, 18% (w/v) Ficoll type 4000, 0.25% (w/v) bromophenol blue, 0.25% (w/v) xylene cyanol) was added to the samples. Electrophoresis of samples was performed at 1V/cm on an 0.8% alkaline agarose gel (50mM NaOH, 1mM EDTA) for 22h. Alkaline gel was neutralized in 1M Tris HCl pH 8.0, 1.5 M NaCl for 1 hour, stained with Diamond nucleic acid dye (Promega) and visualized using LI-COR Odyssey Fc imaging system (LI-COR).

Cell proliferation assay: Astrocyte were seeded into a 96 well (5,000 cells per well) in a DMEM/F12 supplemented media at 37°C and 5%CO_2. Cells were harvested on each indicated day. Proliferation was measured using CyQUANT cell proliferation assay kit (Invitrogen) according to manufacturer's recommendation. Briefly, cells were frozen at

−80°C for at least one day. Cells were thawed at RT and 200μl of CyQUANT GR dye/cell lysis buffer was added. Cells were resuspended briefly by vortexing. Fluorescence of the samples was measured using fluorescence microplate reader set up with excitation and emission filters for GFP. For neural stem cells, proliferation was assessed using trypan blue exclusion every 7 day. 0.5 $\times 10^6$ neural stem cells were plated in T25 flasks and incubated at 37°C and 5%CO_2 incubator. On day 7, cells were spun and counted using a Countess automated cell counter (Invitrogen). Dead cells were identified and excluded using trypan blue. 0.5 $\times 10^6$ cells were again seeded and subsequently counted at every 7 days till passage 5. Proliferation is presented as a cumulative cell counts. Experiments were performed in triplicate.

RNA-seq: Total RNA was isolated from tissue with TRIzol (Invitrogen) and the TruSeq Stranded RNA Kit (Illumina) was used for PolyA+ enrichment and library preparation: Double stranded cDNA fragments were ligated with Illumina paired-end adaptors, followed by size selection (~200bp) and libraries were analyzed using a HiSeq 2000 sequencing system (Illumina). Sequencing reads were quality filtered using TrimGalore (https://www.bioinformatics.babraham.ac.uk/projects/trim_galore/). Filtered reads were aligned to NCBIM37 using BWA (Li and Durbin, 2009), samtools (Li et al., 2009) and STAR (Dobin et al., 2013). Gene counts were quantified using HTSeq (Anders et al., 2015). Differential expression analysis was performed using limma-voom (Ritchie et al., 2015). N=5–7 biological replicates.

GSEA: Gene level fragments per kilobase of transcript per million (FPKM) values were used for gene set enrichment analysis with GSEA version 3.0 (Mootha et al., 2003; Subramanian et al., 2001). Specifically, we used “-metric signal2noise -set_min 4 -permute gene_set”. GSEA FDR 25% cutoff was applied to examine enriched gene sets. Primary gene sets investigated were obtained from MSigDB, and other published data (Rosenberg et al., 2018). Additionally, gene sets for transcriptional analysis were identified using the most differentially expressed genes for specific comparisons to Enrichr (Kuleshov et al., 2016) then downloading libraries and using as them as the gene set for GSEA. Single-sample gene set variation analysis (GSVA) was performed using genes that were enriched for specific cell types in the brain (Hanzelmann et al., 2013; McKenzie et al., 2018).

Quantification and statistical analysis:

Fiji-Image J software (Schindelin et al., 2012) was used for quantification of images. Quantification analysis for various staining was achieved by calculating positive immunosignal in matched sections from at least 3 biological replicates. Bar graph data is represented as mean ± s.e.m. Statistics were calculated using unpaired two-tailed Student’s t test for two groups. GraphPad Prism was used to generate graphs and statistical analyses. p value <0.05 is considered statistically significant.

Supplementary Material

Refer to Web version on PubMed Central for supplementary material.

Acknowledgements.

We thank all members of the McKinnon laboratory for their suggestions and comments; we thank Dr. Jingfeng Zhao for genotyping and technical help, the Animal Resource Center, the Small Animal Imaging Center, the Cytogenetics Core and the Transgenic Core Unit. The Cell and Tissue Imaging Center provided help with microscopy; Flow Cytometry for cell sorting and analysis. PJM is supported by the NIH (NS-37956, CA-21765), the CCSG (P30 CA21765) and the American Lebanese and Syrian Associated Charities of St. Jude Children's Research Hospital.

References.

Abdel-Salam GM, Zaki MS, Lebon P, and Meguid NA (2004). Aicardi-Goutieres syndrome: clinical and neuroradiological findings of 10 new cases. Acta Paediatr 93, 929–936. [PubMed: 15303808]

Aicardi J, and Goutieres F (1984). A progressive familial encephalopathy in infancy with calcifications of the basal ganglia and chronic cerebrospinal fluid lymphocytosis. Ann Neurol 15, 49–54. [PubMed: 6712192]

Akwa Y, Hassett DE, Eloranta ML, Sandberg K, Masliah E, Powell H, Whitton JL, Bloom FE, and Campbell IL (1998). Transgenic expression of IFN-alpha in the central nervous system of mice protects against lethal neurotropic viral infection but induces inflammation and neurodegeneration. J Immunol 161, 5016–5026. [PubMed: 9794439]

Amon JD, and Koshland D (2016). RNase H enables efficient repair of R-loop induced DNA damage. Elife 5.

Anders S, Pyl PT, and Huber W (2015). HTSeq--a Python framework to work with high-throughput sequencing data. Bioinformatics 31, 166–169. [PubMed: 25260700]

Balmus G, Pilger D, Coates J, Demir M, Sczaniecka-Clift M, Barros AC, Woods M, Fu B, Yang F, Chen E, et al. (2019). ATM orchestrates the DNA-damage response to counter toxic non-homologous end-joining at broken replication forks. Nat Commun 10, 87. [PubMed: 30622252]

Bartok E, and Hartmann G (2020). Immune Sensing Mechanisms that Discriminate Self from Altered Self and Foreign Nucleic Acids. Immunity 53, 54–77. [PubMed: 32668228]

Bartsch K, Damme M, Regen T, Becker L, Garrett L, Holter SM, Knittler K, Borowski C, Waisman A, Glatzel M, et al. (2018). RNase H2 Loss in Murine Astrocytes Results in Cellular Defects Reminiscent of Nucleic Acid-Mediated Autoinflammation. Front Immunol 9, 587. [PubMed: 29662492]

Behrendt R, Schumann T, Gerbaulet A, Nguyen LA, Schubert N, Alexopoulou D, Berka U, Lienenklaus S, Peschke K, Gibbert K, et al. (2013). Mouse SAMHD1 Has Antiretroviral Activity and Suppresses a Spontaneous Cell-Intrinsic Antiviral Response. Cell Reports 4, 689–696. [PubMed: 23972988]

Bouwman BAM, and Crosetto N (2018). Endogenous DNA Double-Strand Breaks during DNA Transactions: Emerging Insights and Methods for Genome-Wide Profiling. Genes (Basel) 9.

Boxx GM, and Cheng G (2016). The Roles of Type I Interferon in Bacterial Infection. Cell Host Microbe 19, 760–769. [PubMed: 27281568]

Britton S, Chanut P, Delteil C, Barboule N, Frit P, and Calsou P (2020). ATM antagonizes NHEJ proteins assembly and DNA-ends synapsis at single-ended DNA double strand breaks. Nucleic Acids Res 48, 9710–9723. [PubMed: 32890395]

Campbell IL, Krucker T, Steffensen S, Akwa Y, Powell HC, Lane T, Carr DJ, Gold LH, Henriksen SJ, and Siggins GR (1999). Structural and functional neuropathology in transgenic mice with CNS expression of IFN-alpha. Brain Res 835, 46–61. [PubMed: 10448195]

Cerritelli SM, and Crouch RJ (2009). Ribonuclease H: the enzymes in eukaryotes. FEBS J 276, 1494–1505. [PubMed: 19228196]

Chon H, Vassilev A, DePamphilis ML, Zhao Y, Zhang J, Burgers PM, Crouch RJ, and Cerritelli SM (2009). Contributions of the two accessory subunits, RNASEH2B and RNASEH2C, to the activity and properties of the human RNase H2 complex. Nucleic Acids Res 37, 96–110. [PubMed: 19015152]

Colonna M, and Butovsky O (2017). Microglia Function in the Central Nervous System During Health and Neurodegeneration. Annu Rev Immunol 35, 441–468. [PubMed: 28226226]

Cortez D (2019). Replication-Coupled DNA Repair. Mol Cell 74, 866–876. [PubMed: 31173722]

Crow YJ (2011). Type I interferonopathies: a novel set of inborn errors of immunity. Ann N Y Acad Sci 1238, 91–98. [PubMed: 22129056]

Crow YJ, Chase DS, Lowenstein Schmidt J., Szynkiewicz M, Forte GM, Gornall HL, Oojageer A, Anderson B, Pizzino A, Helman G, et al. (2015). Characterization of human disease phenotypes associated with mutations in TREX1, RNASEH2A, RNASEH2B, RNASEH2C, SAMHD1, ADAR, and IFIH1. Am J Med Genet A 167A, 296–312. [PubMed: 25604658]

Crow YJ, Hayward BE, Parmar R, Robins P, Leitch A, Ali M, Black DN, van Bokhoven H, Brunner HG, Hamel BC, et al. (2006a). Mutations in the gene encoding the 3 ‘−5 ‘ DNA exonuclease TREX1 cause Aicardi-Goutieres syndrome at the AGS1 locus. Nature Genetics 38, 917–920. [PubMed: 16845398]

Crow YJ, Leitch A, Hayward BE, Garner A, Parmar R, Griffith E, Ali M, Semple C, Aicardi J, Babul-Hirji R, et al. (2006b). Mutations in genes encoding ribonuclease H2 subunits cause Aicardi-Goutieres syndrome and mimic congenital viral brain infection. Nat Genet 38, 910–916. [PubMed: 16845400]

Crow YJ, and Manel N (2015). Aicardi-Goutieres syndrome and the type I interferonopathies. Nat Rev Immunol 15, 429–440. [PubMed: 26052098]

DeCarli C, Civitello LA, Brouwers P, and Pizzo PA (1993). The prevalence of computed tomographic abnormalities of the cerebrum in 100 consecutive children symptomatic with the human immune deficiency virus. Ann Neurol 34, 198–205. [PubMed: 8338344]

Dobin A, Davis CA, Schlesinger F, Drenkow J, Zaleski C, Jha S, Batut P, Chaisson M, and Gingeras TR (2013). STAR: ultrafast universal RNA-seq aligner. Bioinformatics 29, 15–21. [PubMed: 23104886]

Dumitrache LC, Shimada M, Downing SM, Kwak YD, Li Y, Illuzzi JL, Russell HR, Wilson DM 3rd, and McKinnon PJ (2018). Apurinic endonuclease-1 preserves neural genome integrity to maintain homeostasis and thermoregulation and prevent brain tumors. Proc Natl Acad Sci U S A 115, E12285–E12294. [PubMed: 30538199]

Frappart PO, Lee Y, Russell HR, Chalhoub N, Wang YD, Orii KE, Zhao J, Kondo N, Baker SJ, and McKinnon PJ (2009). Recurrent genomic alterations characterize medulloblastoma arising from DNA double-strand break repair deficiency. Proc Natl Acad Sci U S A 106, 1880–1885. [PubMed: 19164512]

Gao T, Jernigan J, Raza SA, Dammer EB, Xiao H, Seyfried NT, Levey AI, and Rangaraju S (2019). Transcriptional regulation of homeostatic and disease-associated-microglial genes by IRF1, LXRbeta, and CEBPalpha. Glia 67, 1958–1975. [PubMed: 31301160]

Garau J, Cavallera V, Valente M, Tonduti D, Sproviero D, Zucca S, Battaglia D, Battini R, Bertini E, Cappanera S, et al. (2019). Molecular Genetics and Interferon Signature in the Italian Aicardi Goutieres Syndrome Cohort: Report of 12 New Cases and Literature Review. J Clin Med 8.

Ginhoux F, Greter M, Leboeuf M, Nandi S, See P, Gokhan S, Mehler MF, Conway SJ, Ng LG, Stanley ER, et al. (2010). Fate mapping analysis reveals that adult microglia derive from primitive macrophages. Science 330, 841–845. [PubMed: 20966214]

Gluck S, Guey B, Gulen MF, Wolter K, Kang TW, Schmacke NA, Bridgeman A, Rehwinkel J, Zender L, and Ablasser A (2017). Innate immune sensing of cytosolic chromatin fragments through cGAS promotes senescence. Nature Cell Biology 19, 1061–+. [PubMed: 28759028]

Gunther C, Kind B, Reijns MA, Berndt N, Martinez-Bueno M, Wolf C, Tungler V, Chara O, Lee YA, Hubner N, et al. (2015). Defective removal of ribonucleotides from DNA promotes systemic autoimmunity. J Clin Invest 125, 413–424. [PubMed: 25500883]

Hanzelmann S, Castelo R, and Guinney J (2013). GSVA: gene set variation analysis for microarray and RNA-seq data. BMC Bioinformatics 14, 7. [PubMed: 23323831]

Hartlova A, Erttmann SF, Raffi FA, Schmalz AM, Resch U, Anugula S, Lienenklaus S, Nilsson LM, Kroger A, Nilsson JA, et al. (2015). DNA damage primes the type I interferon system via the cytosolic DNA sensor STING to promote anti-microbial innate immunity. Immunity 42, 332–343. [PubMed: 25692705]

Hiller B, Achleitner M, Glage S, Naumann R, Behrendt R, and Roers A (2012). Mammalian RNase H2 removes ribonucleotides from DNA to maintain genome integrity. J Exp Med 209, 1419–1426. [PubMed: 22802351]

Hopfner KP, and Hornung V (2020). Molecular mechanisms and cellular functions of cGAS-STING signalling. Nat Rev Mol Cell Biol 21, 501–521. [PubMed: 32424334]

Hu MM, and Shu HB (2018). Cytoplasmic Mechanisms of Recognition and Defense of Microbial Nucleic Acids. Annu Rev Cell Dev Biol 34, 357–379. [PubMed: 30095291]

Hu MM, and Shu HB (2020). Innate Immune Response to Cytoplasmic DNA: Mechanisms and Diseases. Annu Rev Immunol 38, 79–98. [PubMed: 31800327]

Jeong HS, Backlund PS, Chen HC, Karavanov AA, and Crouch RJ (2004). RNase H2 of Saccharomyces cerevisiae is a complex of three proteins. Nucleic Acids Research 32, 407–414. [PubMed: 14734815]

Jonkers J, Meuwissen R, van der Gulden H, Peterse H, van der Valk M, and Berns A (2001). Synergistic tumor suppressor activity of BRCA2 and p53 in a conditional mouse model for breast cancer. Nat Genet 29, 418–425. [PubMed: 11694875]

Katyal S, Lee Y, Nitiss KC, Downing SM, Li Y, Shimada M, Zhao J, Russell HR, Petrini JH, Nitiss JL, et al. (2014). Aberrant topoisomerase-1 DNA lesions are pathogenic in neurodegenerative genome instability syndromes. Nat Neurosci 17, 813–821. [PubMed: 24793032]

Kauffman WM, Sivit CJ, Fitz CR, Rakusan TA, Herzog K, and Chandra RS (1992). CT and MR evaluation of intracranial involvement in pediatric HIV infection: a clinical-imaging correlation. AJNR Am J Neuroradiol 13, 949–957. [PubMed: 1590197]

Kellner V, and Luke B (2020). Molecular and physiological consequences of faulty eukaryotic ribonucleotide excision repair. EMBO J 39, e102309. [PubMed: 31833079]

Kierdorf K, Erny D, Goldmann T, Sander V, Schulz C, Perdiguero EG, Wieghofer P, Heinrich A, Riemke P, Holscher C, et al. (2013). Microglia emerge from erythromyeloid precursors via Pu.1- and Irf8-dependent pathways. Nat Neurosci 16, 273–280. [PubMed: 23334579]

Kim N, Huang SN, Williams JS, Li YC, Clark AB, Cho JE, Kunkel TA, Pommier Y, and Jinks-Robertson S (2011). Mutagenic processing of ribonucleotides in DNA by yeast topoisomerase I. Science 332, 1561–1564. [PubMed: 21700875]

Kretschmer S, Wolf C, Konig N, Staroske W, Guck J, Hausler M, Luksch H, Nguyen LA, Kim B, Alexopoulou D, et al. (2015). SAMHD1 prevents autoimmunity by maintaining genome stability. Ann Rheum Dis 74, e17. [PubMed: 24445253]

Kuleshov MV, Jones MR, Rouillard AD, Fernandez NF, Duan Q, Wang Z, Koplev S, Jenkins SL, Jagodnik KM, Lachmann A, et al. (2016). Enrichr: a comprehensive gene set enrichment analysis web server 2016 update. Nucleic Acids Res 44, W90–97. [PubMed: 27141961]

Lebon P, Badoual J, Ponsot G, Goutieres F, Hemeury-Cukier F, and Aicardi J (1988). Intrathecal synthesis of interferon-alpha in infants with progressive familial encephalopathy. J Neurol Sci 84, 201–208. [PubMed: 2837539]

Lee Y, Katyal S, Li Y, El-Khamisy SF, Russell HR, Caldecott KW, and McKinnon PJ (2009). The genesis of cerebellar interneurons and the prevention of neural DNA damage require XRCC1. Nat Neurosci 12, 973–980. [PubMed: 19633665]

Lee Y, and McKinnon PJ (2002). DNA ligase IV suppresses medulloblastoma formation. Cancer Res 62, 6395–6399. [PubMed: 12438222]

Lee Y, Shull ER, Frappart PO, Katyal S, Enriquez-Rios V, Zhao J, Russell HR, Brown EJ, and McKinnon PJ (2012). ATR maintains select progenitors during nervous system development. EMBO J 31, 1177–1189. [PubMed: 22266795]

Lee-Kirsch MA (2017). The Type I Interferonopathies. Annu Rev Med 68, 297–315. [PubMed: 27813875]

Li H, and Durbin R (2009). Fast and accurate short read alignment with Burrows-Wheeler transform. Bioinformatics 25, 1754–1760. [PubMed: 19451168]

Li H, Handsaker B, Wysoker A, Fennell T, Ruan J, Homer N, Marth G, Abecasis G, Durbin R, and Genome Project Data Processing, S. (2009). The Sequence Alignment/Map format and SAMtools. Bioinformatics 25, 2078–2079. [PubMed: 19505943]

Li T, and Chen ZJ (2018). The cGAS-cGAMP-STING pathway connects DNA damage to inflammation, senescence, and cancer. J Exp Med 215, 1287–1299. [PubMed: 29622565]

Livingston JH, and Crow YJ (2016). Neurologic Phenotypes Associated with Mutations in TREX1, RNASEH2A, RNASEH2B, RNASEH2C, SAMHD1, ADAR1, and IFIH1: Aicardi-Goutieres Syndrome and Beyond. Neuropediatrics 47, 355–360. [PubMed: 27643693]

Mackenzie KJ, Carroll P, Lettice L, Tarnauskaite Z, Reddy K, Dix F, Revuelta A, Abbondati E, Rigby RE, Rabe B, et al. (2016). Ribonuclease H2 mutations induce a cGAS/STING-dependent innate immune response. EMBO J 35, 831–844. [PubMed: 26903602]

Magdalou I, Lopez BS, Pasero P, and Lambert SA (2014). The causes of replication stress and their consequences on genome stability and cell fate. Semin Cell Dev Biol 30, 154–164. [PubMed: 24818779]

Masuda T, Iwamoto S, Mikuriya S, Tozaki-Saitoh H, Tamura T, Tsuda M, and Inoue K (2015). Transcription factor IRF1 is responsible for IRF8-mediated IL-1beta expression in reactive microglia. J Pharmacol Sci 128, 216–220. [PubMed: 26318672]

Masuda T, Tsuda M, Yoshinaga R, Tozaki-Saitoh H, Ozato K, Tamura T, and Inoue K (2012). IRF8 is a critical transcription factor for transforming microglia into a reactive phenotype. Cell Rep 1, 334–340. [PubMed: 22832225]

Mathys H, Adaikkan C, Gao F, Young JZ, Manet E, Hemberg M, De Jager PL, Ransohoff RM, Regev A, and Tsai LH (2017). Temporal Tracking of Microglia Activation in Neurodegeneration at Single-Cell Resolution. Cell Reports 21, 366–380. [PubMed: 29020624]

McElhinny SAN, Watts BE, Kumar D, Watt DL, Lundstrom EB, Burgers PMJ, Johansson E, Chabes A, and Kunkel TA (2010). Abundant ribonucleotide incorporation into DNA by yeast replicative polymerases. Proceedings of the National Academy of Sciences of the United States of America 107, 4949–4954. [PubMed: 20194773]

McKenzie AT, Wang M, Hauberg ME, Fullard JF, Kozlenkov A, Keenan A, Hurd YL, Dracheva S, Casaccia P, Roussos P, et al. (2018). Brain Cell Type Specific Gene Expression and Co-expression Network Architectures. Sci Rep 8, 8868. [PubMed: 29892006]

McKinnon PJ (2012). ATM and the molecular pathogenesis of ataxia telangiectasia. Annu Rev Pathol 7, 303–321. [PubMed: 22035194]

McKinnon PJ (2013). Maintaining genome stability in the nervous system. Nat Neurosci 16, 1523–1529. [PubMed: 24165679]

McKinnon PJ (2017). Genome integrity and disease prevention in the nervous system. Genes Dev 31, 1180–1194. [PubMed: 28765160]

McNab F, Mayer-Barber K, Sher A, Wack A, and O'Garra A (2015). Type I interferons in infectious disease. Nat Rev Immunol 15, 87–103. [PubMed: 25614319]

Mesev EV, LeDesma RA, and Ploss A (2019). Decoding type I and III interferon signalling during viral infection. Nat Microbiol 4, 914–924. [PubMed: 30936491]

Mootha VK, Lindgren CM, Eriksson KF, Subramanian A, Sihag S, Lehar J, Puigserver P, Carlsson E, Ridderstrale M, Laurila E, et al. (2003). PGC-1alpha-responsive genes involved in oxidative phosphorylation are coordinately downregulated in human diabetes. Nat Genet 34, 267–273. [PubMed: 12808457]

Morita M, Stamp G, Robins P, Dulic A, Rosewell I, Hrivnak G, Daly G, Lindahl T, and Barnes DE (2004). Gene-targeted mice lacking the Trex1 (DNase III) 3 '-> 5 ' DNA exonuclease develop inflammatory myocarditis. Molecular and Cellular Biology 24, 6719–6727. [PubMed: 15254239]

Motwani M, Pesiridis S, and Fitzgerald KA (2019). DNA sensing by the cGAS-STING pathway in health and disease. Nat Rev Genet 20, 657–674. [PubMed: 31358977]

Nakad R, and Schumacher B (2016). DNA Damage Response and Immune Defense: Links and Mechanisms. Front Genet 7, 147. [PubMed: 27555866]

Nakamura K, Kustatscher G, Alabert C, Hodl M, Forne I, Volker-Albert M, Satpathy S, Beyer TE, Mailand N, Choudhary C, et al. (2021). Proteome dynamics at broken replication forks reveal a distinct ATM-directed repair response suppressing DNA double-strand break ubiquitination. Mol Cell.

Nastasi C, Mannarino L, and D'Incalci M (2020). DNA Damage Response and Immune Defense. Int J Mol Sci 21.

Nayak D, Roth TL, and McGavern DB (2014). Microglia development and function. Annu Rev Immunol 32, 367–402. [PubMed: 24471431]

Park K, Ryoo J, Jeong H, Kim M, Lee S, Hwang SY, Ahn J, Kim D, Moon HC, Baek D, et al. (2021). Aicardi-Goutieres syndrome-associated gene SAMHD1 preserves genome integrity by preventing R-loop formation at transcription-replication conflict regions. PLoS Genet 17, e1009523. [PubMed: 33857133]

Patel AG, Flatten KS, Peterson KL, Beito TG, Schneider PA, Perkins AL, Harki DA, and Kaufmann SH (2016). Immunodetection of human topoisomerase I-DNA covalent complexes. Nucleic Acids Res 44, 2816–2826. [PubMed: 26917015]

Perrino FW, Harvey S, Shaban NM, and Hollis T (2009). RNaseH2 mutants that cause Aicardi-Goutieres syndrome are active nucleases. J Mol Med (Berl) 87, 25–30. [PubMed: 19034401]

Peschke K, Achleitner M, Frenzel K, Gerbaulet A, Ada SR, Zeller N, Lienenklaus S, Lesche M, Poulet C, Naumann R, et al. (2016). Loss of Trex1 in Dendritic Cells Is Sufficient To Trigger Systemic Autoimmunity. Journal of Immunology 197, 2157–2166.

Pokatayev V, Hasin N, Chon H, Cerritelli SM, Sakhuja K, Ward JM, Morris HD, Yan N, and Crouch RJ (2016). RNase H2 catalytic core Aicardi-Goutieres syndrome-related mutant invokes cGAS-STING innate immune-sensing pathway in mice. J Exp Med 213, 329–336. [PubMed: 26880576]

Pommier Y, Sun Y, Huang SN, and Nitiss JL (2016). Roles of eukaryotic topoisomerases in transcription, replication and genomic stability. Nat Rev Mol Cell Biol 17, 703–721. [PubMed: 27649880]

Quek H, Luff J, Cheung K, Kozlov S, Gatei M, Lee CS, Bellingham MC, Noakes PG, Lim YC, Barnett NL, et al. (2017). A rat model of ataxia-telangiectasia: evidence for a neurodegenerative phenotype. Hum Mol Genet 26, 109–123. [PubMed: 28007901]

Rankin LC, and Artis D (2018). Beyond Host Defense: Emerging Functions of the Immune System in Regulating Complex Tissue Physiology. Cell 173, 554–567. [PubMed: 29677509]

Rehwinkel J, Maelfait J, Rigby R, Bridgeman A, and Sousa CRE (2013). SAMHD1-dependent retroviral control and escape in mice. Retrovirology 10, S28–S28.

Reijns MA, Bubeck D, Gibson LC, Graham SC, Baillie GS, Jones EY, and Jackson AP (2011). The structure of the human RNase H2 complex defines key interaction interfaces relevant to enzyme function and human disease. J Biol Chem 286, 10530–10539. [PubMed: 21177854]

Reijns MA, Rabe B, Rigby RE, Mill P, Astell KR, Lettice LA, Boyle S, Leitch A, Keighren M, Kilanowski F, et al. (2012). Enzymatic removal of ribonucleotides from DNA is essential for mammalian genome integrity and development. Cell 149, 1008–1022. [PubMed: 22579044]

Rice G, Patrick T, Parmar R, Taylor CF, Aeby A, Aicardi J, Artuch R, Montalto SA, Bacino CA, Barroso B, et al. (2007). Clinical and molecular phenotype of Aicardi-Goutieres syndrome. Am J Hum Genet 81, 713–725. [PubMed: 17846997]

Rice GI, Bond J, Asipu A, Brunette RL, Manfield IW, Carr IM, Fuller JC, Jackson RM, Lamb T, Briggs TA, et al. (2009). Mutations involved in Aicardi-Goutieres syndrome implicate SAMHD1 as regulator of the innate immune response. Nature Genetics 41, 829–U889. [PubMed: 19525956]

Rice GI, Duany YD, Jenkinson EM, Forte GMA, Anderson BH, Ariaudo G, Bader-Meunier B, Baildam EM, Battini R, Beresford MW, et al. (2014). Gain-of-function mutations in IFIH1 cause a spectrum of human disease phenotypes associated with upregulated type I interferon signaling. Nature Genetics 46, 503–509. [PubMed: 24686847]

Rice GI, Forte GM, Szynkiewicz M, Chase DS, Aeby A, Abdel-Hamid MS, Ackroyd S, Allcock R, Bailey KM, Balottin U, et al. (2013). Assessment of interferon-related biomarkers in Aicardi-Goutieres syndrome associated with mutations in TREX1, RNASEH2A, RNASEH2B, RNASEH2C, SAMHD1, and ADAR: a case-control study. Lancet Neurol 12, 1159–1169. [PubMed: 24183309]

Rice GI, Kasher PR, Forte GMA, Mannion NM, Greenwood SM, Szynkiewicz M, Dickerson JE, Bhaskar SS, Zampini M, Briggs TA, et al. (2012). Mutations in ADAR1 cause Aicardi-Goutieres syndrome associated with a type I interferon signature. Nature Genetics 44, 1243–1248. [PubMed: 23001123]

Ritchie ME, Phipson B, Wu D, Hu Y, Law CW, Shi W, and Smyth GK (2015). limma powers differential expression analyses for RNA-sequencing and microarray studies. Nucleic Acids Res 43, e47. [PubMed: 25605792]

Roers A, Hiller B, and Hornung V (2016). Recognition of Endogenous Nucleic Acids by the Innate Immune System. Immunity 44, 739–754. [PubMed: 27096317]

Rohman MS, Koga Y, Takano K, Chon H, Crouch RJ, and Kanaya S (2008). Effect of the disease-causing mutations identified in human ribonuclease (RNase) H2 on the activities and stabilities of yeast RNase H2 and archaeal RNase HII. FEBS J 275, 4836–4849. [PubMed: 18721139]

Rosenberg AB, Roco CM, Muscat RA, Kuchina A, Sample P, Yao Z, Graybuck LT, Peeler DJ, Mukherjee S, Chen W, et al. (2018). Single-cell profiling of the developing mouse brain and spinal cord with split-pool barcoding. Science 360, 176–182. [PubMed: 29545511]

Sase S, Takanohashi A, Vanderver A, and Almad A (2018). Astrocytes, an active player in Aicardi-Goutieres syndrome. Brain Pathology 28, 399–407. [PubMed: 29740948]

Schindelin J, Arganda-Carreras I, Frise E, Kaynig V, Longair M, Pietzsch T, Preibisch S, Rueden C, Saalfeld S, Schmid B, et al. (2012). Fiji: an open-source platform for biological-image analysis. Nat Methods 9, 676–682. [PubMed: 22743772]

Schmittgen TD, and Livak KJ (2008). Analyzing real-time PCR data by the comparative C(T) method. Nat Protoc 3, 1101–1108. [PubMed: 18546601]

Sekiguchi J, and Shuman S (1997). Site-specific ribonuclease activity of eukaryotic DNA topoisomerase I. Mol Cell 1, 89–97. [PubMed: 9659906]

Song X, Ma F, and Herrup K (2019). Accumulation of Cytoplasmic DNA Due to ATM Deficiency Activates the Microglial Viral Response System with Neurotoxic Consequences. J Neurosci 39, 6378–6394. [PubMed: 31189575]

Sparks JL, Chon H, Cerritelli SM, Kunkel TA, Johansson E, Crouch RJ, and Burgers PM (2012). RNase H2-initiated ribonucleotide excision repair. Mol Cell 47, 980–986. [PubMed: 22864116]

Subramanian D, Furbee CS, and Muller MT (2001). ICE bioassay. Isolating in vivo complexes of enzyme to DNA. Methods Mol Biol 95, 137–147. [PubMed: 11089227]

Tan X, Sun L, Chen J, and Chen ZJ (2018). Detection of Microbial Infections Through Innate Immune Sensing of Nucleic Acids. Annu Rev Microbiol 72, 447–478. [PubMed: 30200854]

Uehara R, Cerritelli SM, Hasin N, Sakhuja K, London M, Iranzo J, Chon H, Grinberg A, and Crouch RJ (2018). Two RNase H2 Mutants with Differential rNMP Processing Activity Reveal a Threshold of Ribonucleotide Tolerance for Embryonic Development. Cell Rep 25, 1135–1145 e1135. [PubMed: 30380406]

Uggenti C, Lepelley A, and Crow YJ (2019). Self-Awareness: Nucleic Acid-Driven Inflammation and the Type I Interferonopathies. Annu Rev Immunol 37, 247–267. [PubMed: 30633609]

van Heteren JT, Rozenberg F, Aronica E, Troost D, Lebon P, and Kuijpers TW (2008). Astrocytes produce interferon-alpha and CXCL10, but not IL-6 or CXCL8, in Aicardi-Goutieres syndrome. Glia 56, 568–578. [PubMed: 18240301]

Williams JS, and Kunkel TA (2014). Ribonucleotides in DNA: origins, repair and consequences. DNA Repair (Amst) 19, 27–37. [PubMed: 24794402]

Williams JS, Lujan SA, and Kunkel TA (2016). Processing ribonucleotides incorporated during eukaryotic DNA replication. Nat Rev Mol Cell Biol 17, 350–363. [PubMed: 27093943]

Xu Y (2006). DNA damage: a trigger of innate immunity but a requirement for adaptive immune homeostasis. Nat Rev Immunol 6, 261–270. [PubMed: 16498454]

Yang H, Wang HZ, Ren JY, Chen Q, and Chen ZJJ (2017). cGAS is essential for cellular senescence. Proceedings of the National Academy of Sciences of the United States of America 114, E4612–E4620. [PubMed: 28533362]

Yang YG, Lindahl T, and Barnes DE (2007). Trex1 exonuclease degrades ssDNA to prevent chronic checkpoint activation and autoimmune disease. Cell 131, 873–886. [PubMed: 18045533]

Zeman MK, and Cimprich KA (2014). Causes and consequences of replication stress. Nat Cell Biol 16, 2–9. [PubMed: 24366029]

Zhou N, Liu K, Sun Y, Cao Y, and Yang J (2019). Transcriptional mechanism of IRF8 and PU.1 governs microglial activation in neurodegenerative condition. Protein Cell 10, 87–103. [PubMed: 30484118]

Highlights.

1. RNASEH2 is necessary for neurogenesis and prevention of neuroinflammation.
2. ATM suppresses the neural impact of *Rnaseh2* inactivation.
3. Neuropathology from disabled RNASEH2B is rescued by p53 but not cGAS inactivation.

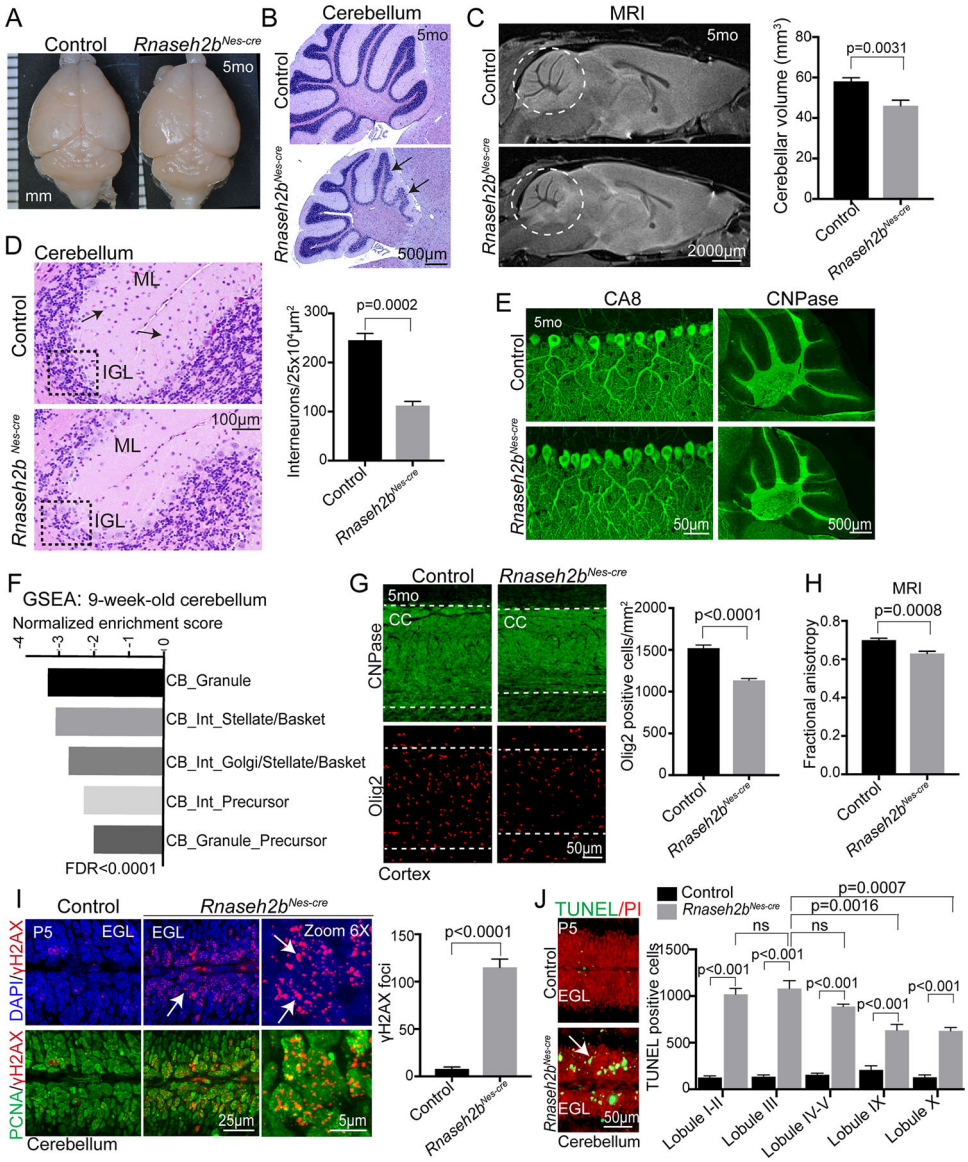

Figure 1: RNASEH2 deficiency in the mouse nervous system recapitulates AGS.

(A) Comparative images of WT and *Rnaseh2b*$^{Nes\text{-}cre}$ brain. (B) H&E shows loss of granule neurons in the *Rnaseh2b*$^{Nes\text{-}cre}$ cerebellum, particularly in the anterior cerebellum (arrows). (C) MRI volumetric analysis shows a significant reduction in the size of the cerebellum occurs after RNASEH2B inactivation (white circle). (D) H&E staining reveals loss of granule cells and interneurons in the *Rnaseh2b*$^{Nes\text{-}cre}$ cerebellum (arrows). Graph shows interneuron quantification; IGL is internal granule layer and ML is molecular layer. Boxed areas show comparative granule neuron density. (E) Purkinje cells and oligodendrocytes appear unaffected by RNASEH2B deficiency as shown by CA8 and CNPase immunostaining. (F) Gene Set Enrichment Analysis (GSEA) of RNA-seq from 9-week-old control and *Rnaseh2b*$^{Nes\text{-}cre}$ cerebellum identifies underrepresentation of genes related to granule and interneuron cells in the mutant cerebellum. (G) In the *Rnaseh2b*$^{Nes\text{-}cre}$ cortex, a thinning of the corpus callosum (CC) and reduction in oligodendrocytes is

observed using CNPase and Olig2 immunostaining, respectively. Olig2 in the corpus callosum is significantly reduced in the *Rnaseh2b*$^{Nes\text{-}cre}$ cortex. (H) MRI-diffusion tensor imaging of 5-month-old *Rnaseh2b*$^{Nes\text{-}cre}$ brains display reduced white matter (corpus callosum) fractional anisotropy. (I) γH2AX immunostaining reveals DNA damage in the P5 cerebellar EGL (arrows); quantified in adjacent graph. PCNA marks proliferative cells. (J) TUNEL staining reveals RNASEH2B inactivation causes cell death in the P5 cerebellum (arrows). The number of TUNEL positive cells/mm^2 varies between anterior and posterior cerebellar lobules in *Rnaseh2b*$^{Nes\text{-}cre}$ mice indicating disproportionate cell loss. All graphical data are mean ± s.e.m. See also Figure S1 and Tables S1, S2.

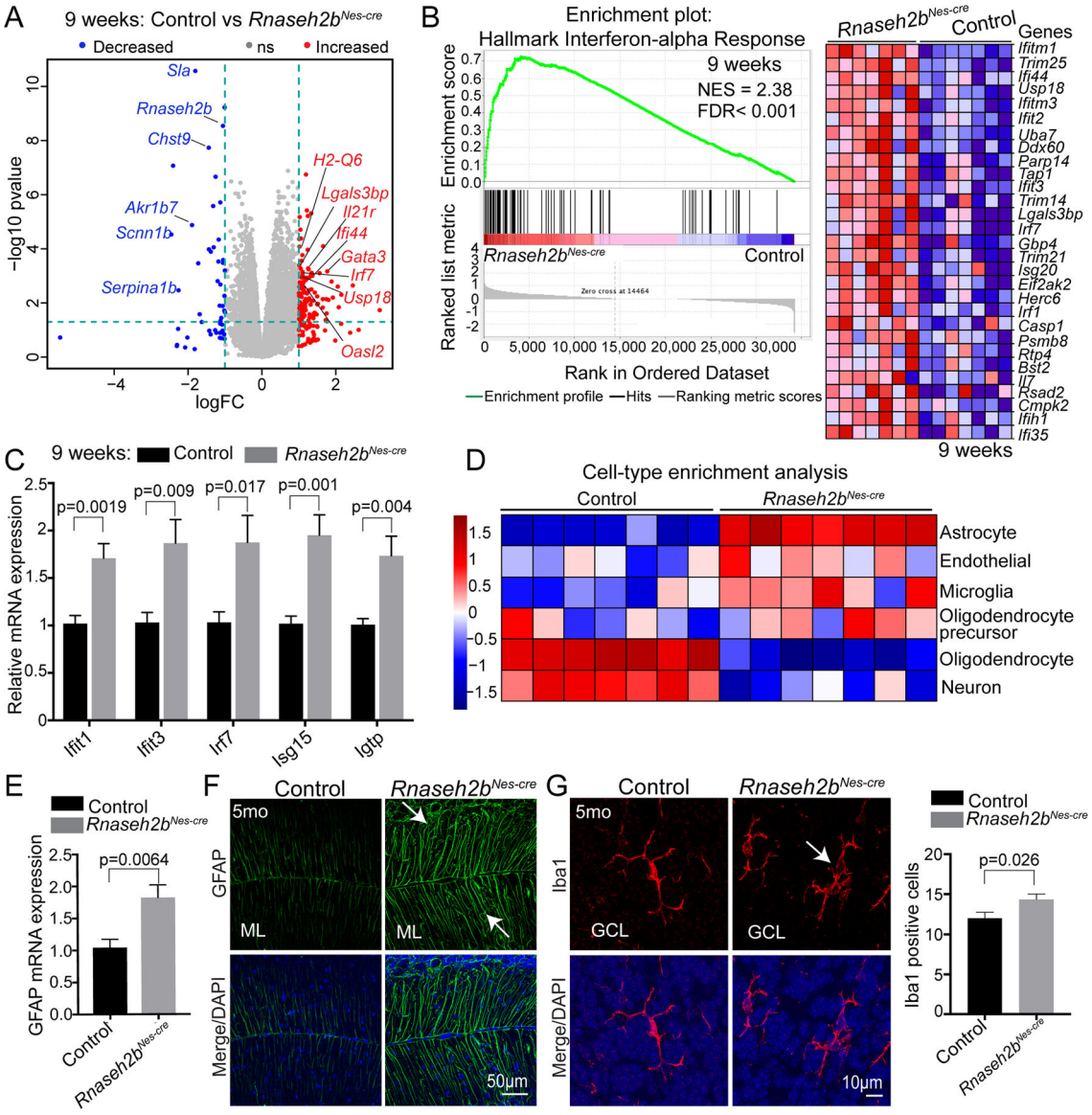

Figure 2: Induction of type I interferon and inflammation in the *Rnaseh2b*$^{Nes\text{-}cre}$ nervous system.

(A) Volcano plot of RNA-seq data shows genes with increased (red) and decreased (blue) expression in *Rnaseh2b*$^{Nes\text{-}cre}$ cerebellum compared to control tissue. Representative genes are listed. Dashed vertical lines demarcate $Log_2FC > 1$ or -1. Dashed green line corresponds to p-value of 0.05. (B) GSEA analysis shows significant enrichment of hallmark type I interferon alpha pathway genes in adult *Rnaseh2b*$^{Nes\text{-}cre}$ cerebellum compared to control. The adjacent heatmap shows gene expression changes that support the GSEA. (C) Transcript levels of several interferon-responsive genes are increased in *Rnaseh2b*$^{Nes\text{-}cre}$ cerebellum as measured by qPCR; *Gapdh* was used to normalize expression. (D) Heatmap of GSVA cell type enrichment analysis of RNA-seq data indicates enrichment of astrocyte and microglia-enriched genes in the *Rnaseh2b*$^{Nes\text{-}cre}$ cerebellum. (E) qPCR analysis shows increased *Gfap* mRNA in the 9-week-old *Rnaseh2b*$^{Nes\text{-}cre}$ cerebellum compared to control. (F) GFAP immunostaining shows an enhanced activation of astrocytes (arrows) in the *Rnaseh2b*$^{Nes\text{-}cre}$

cerebellum. (G) The microglia marker Iba1 is also elevated in the *Rnaseh2b*$^{Nes\text{-}cre}$ cerebellum; data is ± s.e.m. of Iba1 positive cells. See also Figure S2 and Tables S1, S2, S3.

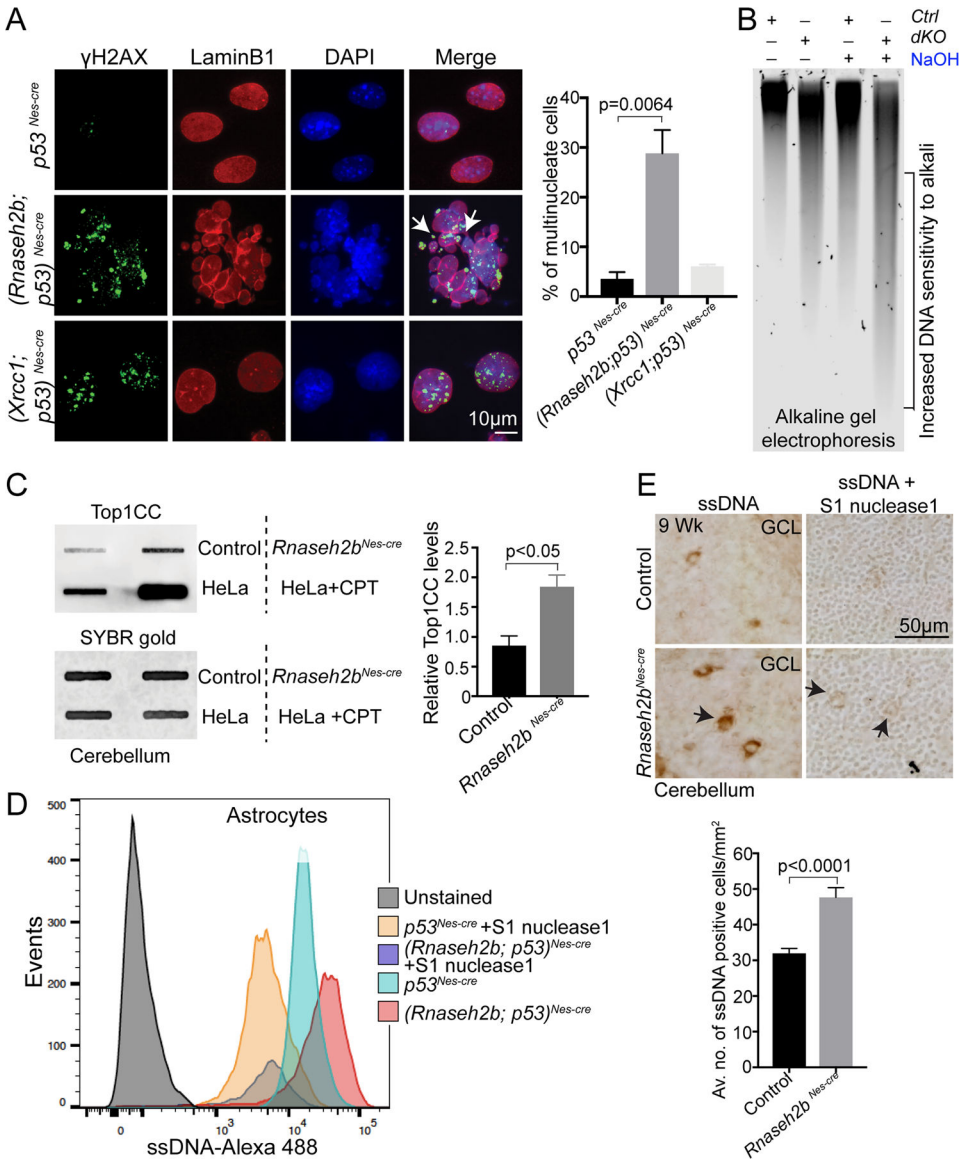

Figure 3: Neural inactivation of RNASEH2B causes DNA damage accumulation.

A) Significant numbers of (*Rnaseh2b;p53)*$^{Nes\text{-}cre}$ cells are multi-nucleated compared to control or (*Xrcc1;p53)*$^{Nes\text{-}cre}$ astrocytes. Immunostaining with LaminB1 and γH2AX antibodies show that these multinucleated cells have lobular nuclear morphology, surrounded by LaminB1 and accumulated DNA damage (arrows). B) Gel electrophoresis reveals enhanced sensitivity of sodium hydroxide (NaOH)-treated genomic DNA from (*Rnaseh2b;p53)*$^{Nes\text{-}cre}$ cells compared to *p53*$^{Nes\text{-}cre}$ cells, consistent with incorporation of ribonucleotides into DNA. (C) RNASEH2B loss results in increased Top1cc in *Rnaseh2b*$^{Nes\text{-}cre}$ cerebellum compared to controls, as quantified using an ICE assay. DNA loading is measured using SYBR Gold. HeLa cells treated with camptothecin (CPT) serve as a positive control for Top1cc formation. (D) Flow cytometry analysis of ssDNA immunostaining using ssDNA antibody shows an enhanced accumulation of cytoplasmic DNA in (*Rnaseh2b;p53)*$^{Nes\text{-}cre}$ compared with *p53*$^{Nes\text{-}cre}$ astrocytes. S1 nuclease abolishes

the ssDNA staining indicating specificity. (E) ssDNA immunostaining shows increased ssDNA positive cells in the *Rnaseh2b*$^{Nes\text{-}cre}$ cerebellum compared to control, while treatment of sections with S1 nuclease reduces ssDNA staining (arrows), indicated in the graph below (mean ± s.e.m.). See also Figure S3.

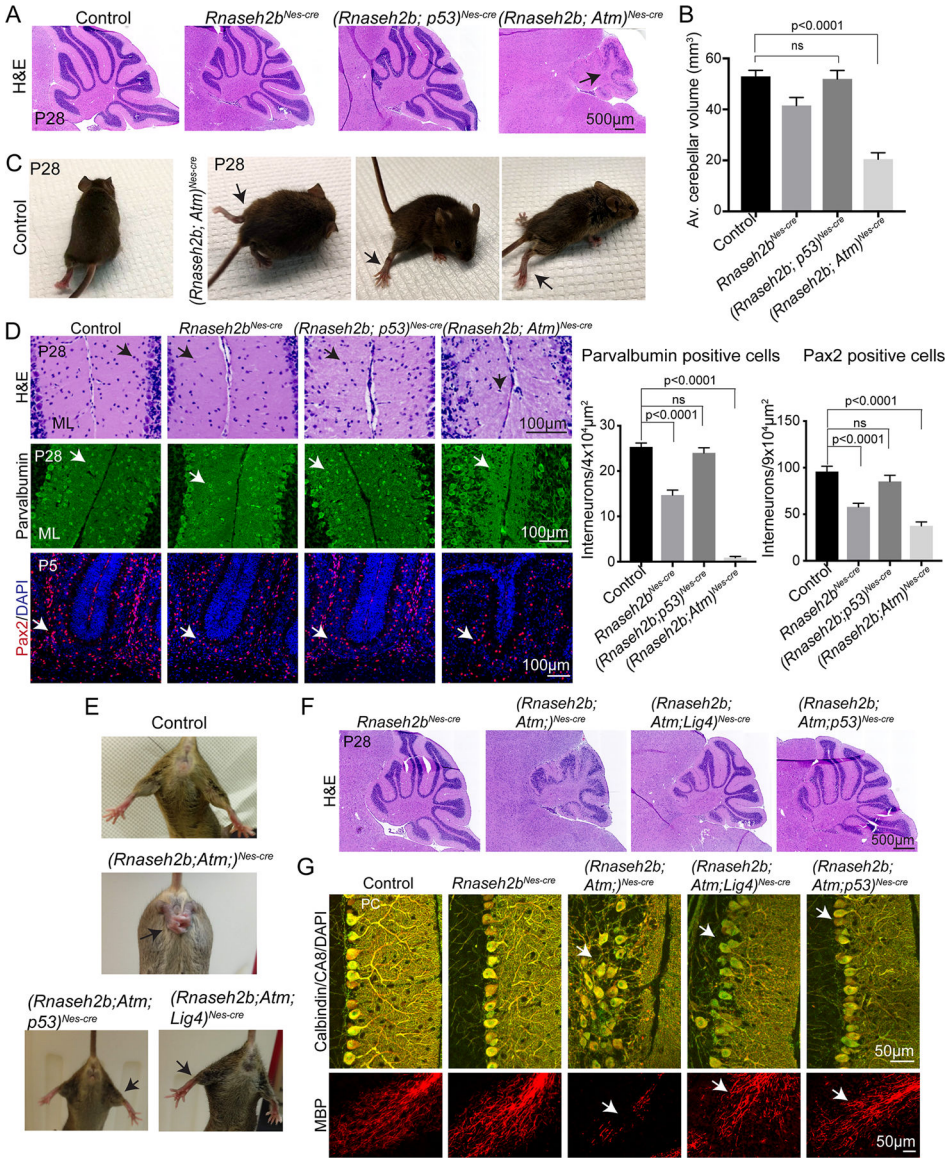

Figure 4: ATM suppresses cerebellar atrophy in the *Rnaseh2b*$^{Nes\text{-}cre}$ brain in a NHEJ-dependent manner.

(A) H&E staining of P28 (*Rnaseh2b*;*Atm*)$^{Nes\text{-}cre}$ shows marked exacerbation of the *Rnaseh2b*$^{Nes\text{-}cre}$ cerebellar phenotype (arrows), while the (*Rnaseh2b*;*p53*)$^{Nes\text{-}cre}$ brain shows rescue of *Rnaseh2b*$^{Nes\text{-}cre}$ cerebellar size. (B) MRI volumetric measurement of P28 mouse brains of respective genotypes indicate a significant reduction of cerebellar volume in the (*Rnaseh2b*;*Atm*)$^{Nes\text{-}cre}$ tissue. (C) Dual inactivation of *Rnaseh2b* and *Atm* in mice causes ataxia (arrows). (D) H&E and immunofluorescence staining using parvalbumin show that p53 deletion, but not ATM, rescues loss of interneurons in *Rnaseh2b*$^{Nes\text{-}cre}$ cerebellum. Pax2 immunostaining for precursors at P5 shows a loss of cerebellar interneuron progenitors in *Rnaseh2b*$^{Nes\text{-}cre}$ cerebellum, which is exacerbated after ATM loss; in contrast, p53 deletion rescues the numbers of Pax2 +ve cells. Quantification is on the adjacent bar graph; mean ± s.e.m. (E-G) Inactivation of the NHEJ pathway by *Lig4* deletion recues neuropathology of (*Rnaseh2b*; *Atm*)$^{Nes\text{-}cre}$ mice. (E) (*Rnaseh2b*;*Atm*)$^{Nes\text{-}cre}$ mice are ataxic and display

hindlimb clasping defects (arrow) that are rescued by inactivation of *Lig4* or *p53*. (F) H&E staining shows rescue of cerebellar size and morphology of (*Rnaseh2b*;*Atm*)$^{Nes\text{-}cre}$ mice after Lig4 or p53 loss. (G) Immunostaining for calbindin/CA8 or MBP illustrates rescue of Purkinje cell organization and myelination defects upon *Lig4* or *p53* inactivation in (*Rnaseh2b*;*Atm*)$^{Nes\text{-}cre}$ mice. ns=not significant; ML=molecular layer. See also Figures S4 and S5.

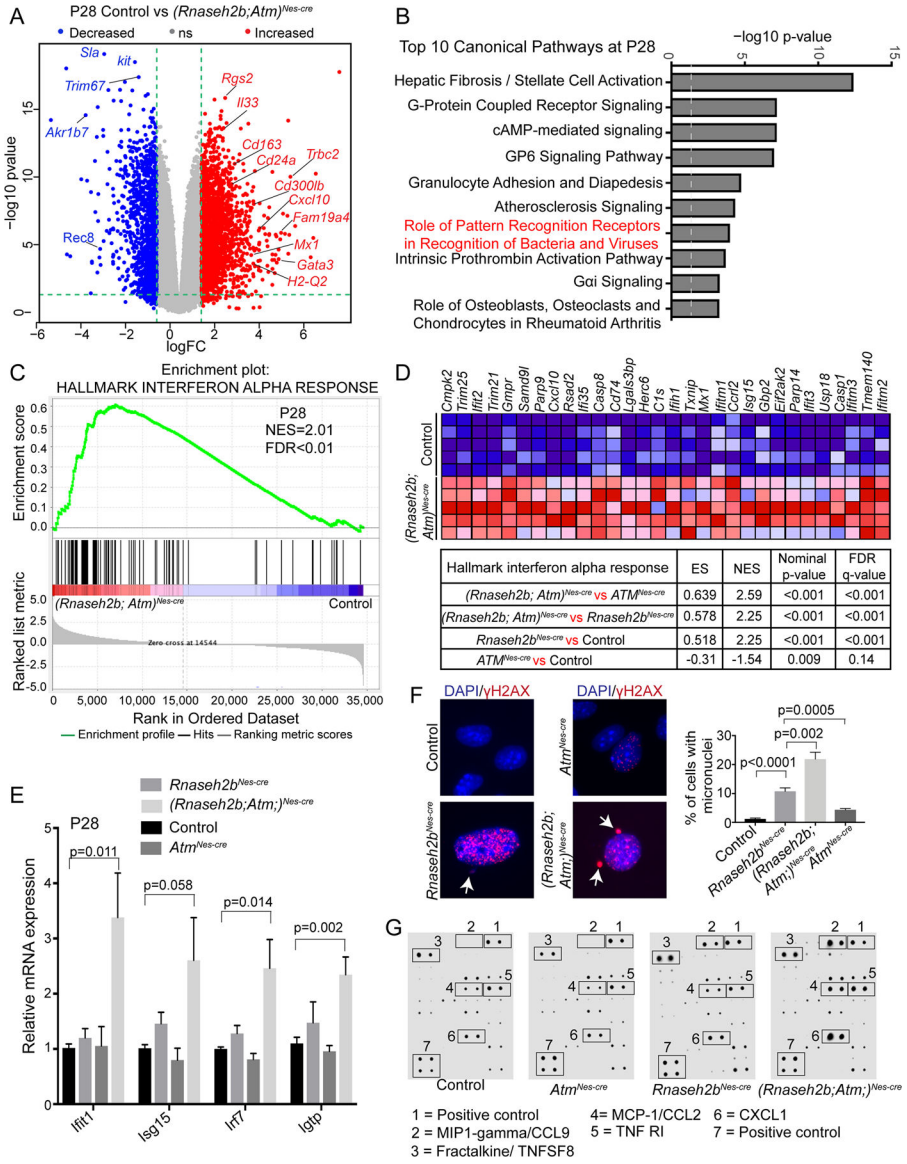

Figure 5: ATM suppresses activation of type I interferon and neuroinflammation in the *Rnaseh2b*$^{Nes\ cre}$ brain.

(A) A volcano plot of RNA-seq analysis shows differentially expressed genes in (*Rnaseh2b*;*Atm*)$^{Nes\text{-cre}}$ cerebellum compared to control. Representative genes are listed. Dashed vertical lines correspond to FC <−1 or >1. Dashed green line corresponds to p value <0.05, and genes above this line are defined as significant. (B) The top 10 most significantly enriched pathway analyzed by ingenuity pathway analysis. (C-D) GSEA analysis shows significant enrichment of hallmark type I interferon alpha pathway genes in adult (*Rnaseh2b*;*Atm*)$^{Nes\text{-}cre}$ cerebellum compared to control. Affected genes that drive enrichment are indicated in the adjacent heatmap. Enrichment scores for various genotype comparisons are shown in the table. (E) Transcript levels of several interferon-responsive genes are increased upon combined loss of ATM and RNASEH2B function as measured by qPCR. (F) *Rnaseh2b*$^{Nes\text{-}cre}$ astrocytes exhibit increased micronuclei formation (arrows) compared to control cells, and this phenotype is amplified upon additional inactivation of

ATM. Micronuclei also accumulates DNA damage as shown by γH2AX immunostaining. (G) Cytokine array analyses of secreted factors in the supernatant of astrocytes from the respective genotypes indicates enhanced release of inflammatory molecules upon combined inactivation of RNASEH2B and ATM. See also Figures S6, S7 and Tables S1, S2.

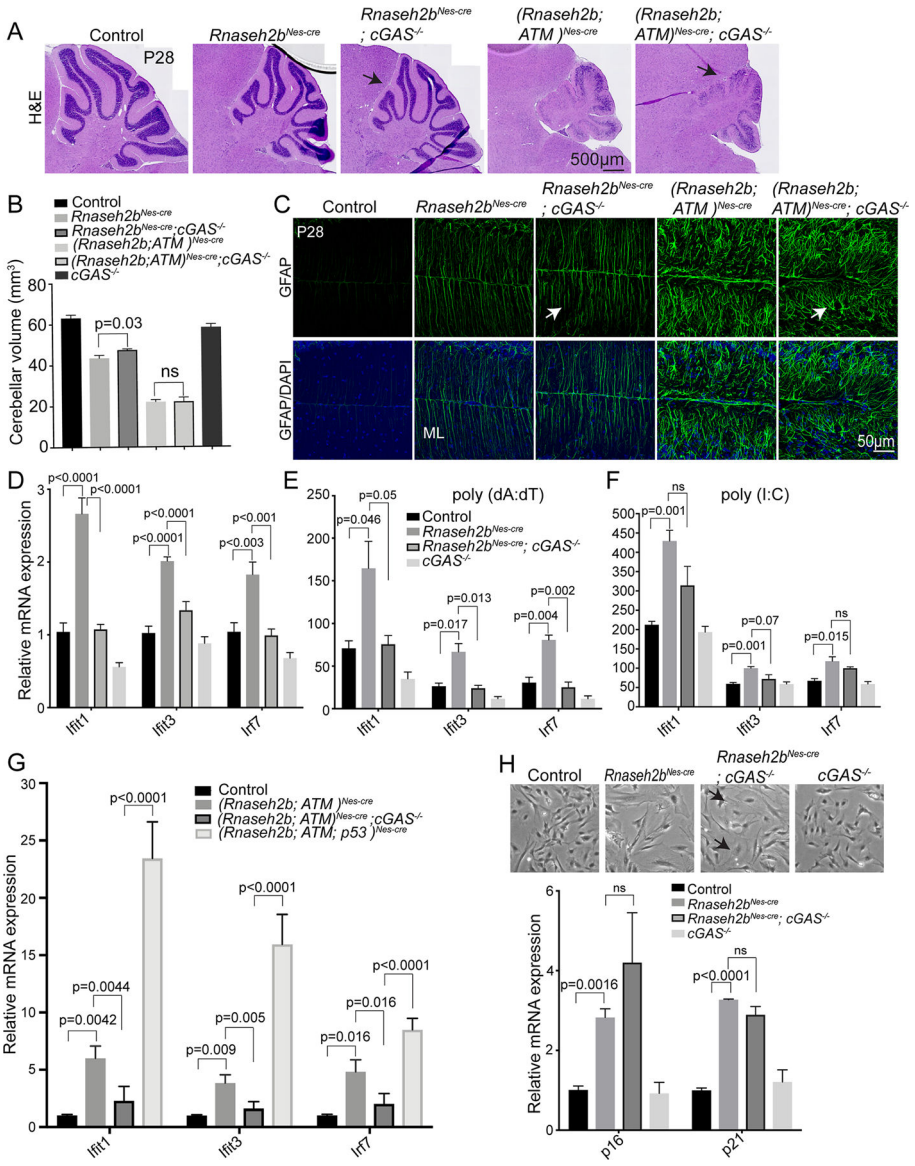

Figure 6: Distinct reactive microglia states occur after neural inactivation of RNASEH2 and ATM.

(A) GFAP immunostaining reveals activation of astrocytes in *Rnaseh2b*$^{Nes\text{-}cre}$, which is further increased in (*Rnaseh2b*;*Atm*)$^{Nes\text{-}cre}$. In (*Rnaseh2b*;*Atm*)$^{Nes\text{-}cre}$ cerebellum, astrocyte morphology is characterized by thickening of cellular processes (arrow). (B) Iba1 immunostaining shows enhanced activation of microglia in (*Rnaseh2b*;*Atm*)$^{Nes\text{-}cre}$ compared to control (arrows). (C) GSEA at P5, P28 and 9 weeks reveal distinct reactive microglia phenotype in the *Rnaseh2b*$^{Nes\text{-}cre}$ and (*Rnaseh2b*;*Atm*)$^{Nes\text{-}cre}$ cerebellum. The majority of IRF8-known consensus targets, but not IRF1, are enriched in the 'late-response' microglia reactive state in *Rnaseh2b*$^{Nes\text{-}cre}$ and (*Rnaseh2b*;*Atm*)$^{Nes\text{-}cre}$ cerebellum compared to controls. FDR <0.05 is considered significant. (D) Correlation analyses between the Log_2FC of *Rnaseh2b*$^{Nes\text{-}cre}$ vs. Control and (*Rnaseh2b*;*Atm*)$^{Nes\text{-}cre}$ vs. Control for individual genes at P28 show the relationship between IRF1 or IRF8 genes vs. that of all genes. IRF8

targets show an increased enrichment in (*Rnaseh2b*;*Atm*)$^{Nes\text{-}cre}$ vs. Control. See also Table S2.

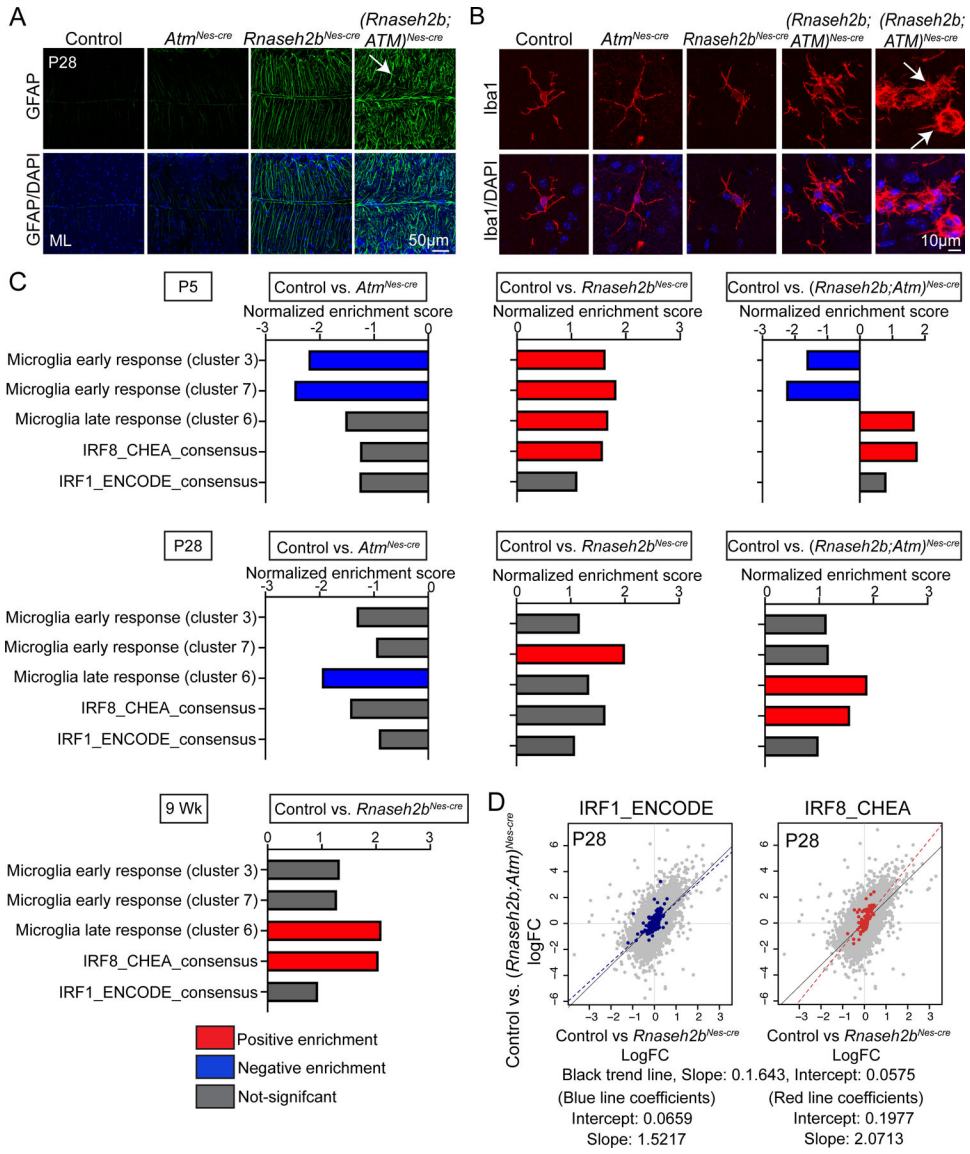

Figure 7: Type I interferon signaling does not mediate *Rnaseh2b*$^{Nes\text{-}cre}$ neuropathology.

(A) H&E staining shows that cGAS deletion only modestly rescues cerebellar size of *Rnaseh2b*$^{Nes\text{-}cre}$ mice, but not in the more affected (*Rnaseh2b*;*Atm*)$^{Nes\text{-}cre}$. (B) MRI analyses of brains of respective genotypes indicate that cGAS inactivation does not rescue the smaller cerebellar size of (*Rnaseh2b*;*Atm*)$^{Nes\text{-}cre}$. (C) GFAP immunostaining shows astrocytosis in *Rnaseh2b*$^{Nes\text{-}cre}$ and (*Rnaseh2b*;*Atm*)$^{Nes\text{-}cre}$ cerebellum, which is not rescued by cGAS deletion. (D) In astrocytes, cGAS inactivation rescues enhanced type I IFN signaling observed after RNASEH2B loss. qPCR analysis shows induction of transcript levels of *Ifit1*,*Ifit3* and *Irf7* upon RNASEH2B depletion, which is rescued by cGAS deletion. (E-F) Stimulation of astrocytes with poly(dA:dT) or poly(I:C) agents results in heightened induction of interferon-stimulated genes, which is rescued by cGAS deletion for poly(dA:dT) (E), but not for poly(I:C) (F). (G) cGAS deletion, but not p53, rescues type I IFN signaling in (*Rnaseh2b*;*Atm*)$^{Nes\text{-}cre}$ astrocytes as evident by qPCR analysis of interferon -stimulated genes. (H) cGAS deletion does not rescue the senescent phenotype

of *Rnaseh2b*$^{Nes\text{-}cre}$ astrocytes. *Rnaseh2b*$^{Nes\text{-}cre}$;*cGAS*$^{-/-}$ astrocytes exhibit flat morphology (arrow), show growth similar to *Rnaseh2b*$^{Nes\text{-}cre}$ cells and show increased expression of *P16* and *P21* transcripts. ns=not significant; ML=molecular layer.

Key resource table

REAGENT or RESOURCE	SOURCE	IDENTIFIER
Antibodies		
Top1	Bethyl Laboratories	Cat#302-590A RRID:AB_2034875
Calbindin	Sigma-Aldrich	Cat#C9848 RRID:AB_476894
CA8	Novus Biologicals	Cat#NB100-74382 RRID:AB_2066278
GFAP	Sigma-Aldrich	Cat#G3893 RRID:AB_477010
γH2AX pSer-139	Cell Signaling Technology	Cat#2577 RRID:AB_2118010
Iba1	Novus Biologicals	Cat#NB100-1028 RRID:AB_521594
NeuN	Millipore	Cat#MAB377 RRID:AB_2298772
Parvalbumin	Millipore	Cat#MAB1572 RRID:AB_2174013
Olig2	Millipore	Cat#AB9610 RRID:AB_570666
ssDNA	Millipore	Cat#MAB3299 RRID:AB_94795
KAP1-pS824	Bethyl Laboratories	Cat#A300-767A RRID:AB_669740
53BP1	Bethyl Laboratories	Cat#A300-272A RRID:AB_185520
PCNA (PC-10)	Santa Cruz Biotechnology	Cat#Sc56 RRID:AB_628110
Top1cc	Millipore	Cat#MABE 1084 RRID:AB_2756354
S9.6	Kerafast	Cat#ENH001 RRID:AB_2687463
Pax2	Invitrogen	Cat#71-6000 RRID:AB_2533990
CNPase	Sigma-Aldrich	Cat#C5922 RRID:AB_476854
MBP	Abcam	Cat#ab40390 RRID:AB_1141521
Alexa fluor 488 donkey anti-mouse IgG	Molecular Probes	Cat#A-21202 RRID:AB_141607
Alexa fluor 488 donkey anti-rabbit IgG	Molecular Probes	Cat#A-21206 RRID:AB_2535792
Alexa fluor 555 donkey anti-mouse IgG	Molecular Probes	Cat#A-31570 RRID:AB_2536180
Alexa fluor 555 donkey anti-rabbit IgG	Molecular Probes	Cat#A-31572 RRID:AB_162543
Alexa fluor 555 donkey anti-goat IgG	Molecular Probes	Cat#A21432 AB_2535853
Alexa fluor 488 donkey anti-rabbit IgM	Molecular Probes	Cat#A21042 RRID:AB_2535711
HRP conjugated anti mouse IgM	Bethyl Laboratories	Cat#A90-201P RRID:AB_10631919
HRP conjugated goat anti-rabbit	Sigma-Aldrich	Cat#NA934 RRID:AB_772206
Bacterial and virus strains		
Biological samples		
Chemicals, peptides, and recombinant proteins		
4% buffered paraformaldehyde	Thermo Scientific	Cat#J19943
Tissue-freezing media	Electron Microscopy Sciences	Cat#72592
HistoVT One	Nacalai tesque	Cat#06380-05
Normal donkey serum	Jackson ImmunoResearch Laboratories	Cat#017-000-121
BSA	Sigma-Aldrich	Cat#A4503
ProLong Gold antifade with DAPI	Invitrogen	Cat#P36931

REAGENT or RESOURCE	SOURCE	IDENTIFIER
Vectashield antifade mounting medium with propidium iodide	Vector Laboratories	Cat#H-1300
DPX mountant	Electron Microscopy Sciences	Cat#13510
S1 nuclease	Invitrogen	Cat#18001016
Ultrapure water with 0.1% Gelatin	Millipore	Cat#ES-006-B
TRIzol	Invitrogen	Cat#A33250
Power SYBR green PCR master mix	Applied Biosystems	Cat#4367659
NeuroCult NSC basal media	STEMCELL Technologies	Cat # 05700
DMEM/F12 (1:1) media	Gibco	Cat#11330-032
FBS	Gibco	Cat#10437028
Recombinant EGF	Millipore	Cat#01-101
poly (I:C)	Invivogen	Cat#tlrl-pic
poly (dA:dT)	Invivogen	Cat#tlrl-patn-1
Xfect transfection reagent	Takara Bio	Cat#631318
Camptothecin	Sigma-Aldrich	Cat#C9911
SYBR Gold	Invitrogen	Cat#S11494
Diamond nucleic acid dye	Promega	Cat#H1181
Critical commercial assays		
ApopTag-fluorescein in situ apoptosis detection kit	Millipore	Cat#S7110
DAB peroxidase substrate kit	Vector Laboratories	Cat #SK-4100
SA-β-Gal staining kit	Cell Signaling Technology	Cat#9860
SuperScript III first-strand synthesis kit	Invitrogen	Cat#18080051
SuperScript IV VILO master mix with ezDNAse enzyme kit	Invitrogen	Cat#11766050
mouse inflammation array C1	Ray Biotech	Cat#AAM-INF-1-8
QIAmp DNA mini kit	Qiagen	Cat#51304
CyQUANT cell proliferation assay kit	Invitrogen	Cat#C7026
Deposited data		
RNA seq raw data	This paper	GEO: GSE181159
Experimental models: Cell lines		
Mouse primary cortical astrocytes	This paper	N/A
Experimental models: Organisms/strains		
Mouse: B6.Cg-Tg(Nes-cre)1Kln/J	The Jackson Laboratory	JAX #003771 RRID:IMSR_JAX:003771
Mouse:B6(C)-*Cgas* $^{tm1d(EUCOMM)Hmgu}$/J	The Jackson Laboratory	JAX #026554 RRID:IMSR_JAX:026554
Mouse embryo: *Rnaseh2b* $^{tm1a(EUCOMM)}$Wtsi	EUCOMM/Welcome Trust Sanger Institute	Cat #05078 RRID:IMSR_EM:05078
Mouse: *Atm* $^{Nes-cre}$	(Lee et al., 2012)	N/A
Mouse: *Lig4* $^{Nes-cre}$	(Frappart et al., 2009)	N/A
Mouse: *p53* $^{Nes-cre}$	(Jonkers et al., 2001)	N/A
Mouse: *Xrcc1* $^{Nes-cre}$	(Lee et al., 2009)	N/A

REAGENT or RESOURCE	SOURCE	IDENTIFIER
Mouse:*Rnaseh2b*$^{Nes\text{-}cre}$	This study	N/A
Oligonucleotides		
qRT-PCR primers	This paper	Table S3
Genotyping primers	This paper	Table S3
Recombinant DNA		
Software and algorithms		
Fiji ImageJ	(Schindelin et al., 2012)	https://imagej.net/software/fiji/
GraphPad Prism 7	GraphPad Software Inc.	https://www.graphpad.com/
GSEA version 3.0	(Mootha et al., 2003; Subramanian et al., 2001)	http://software.broadinstitute.org/gsea/index.jsp
BWA- Burrows-Wheeler Aligner (BWA)	(Li and Durbin, 2009)	http://bio-bwa.sourceforge.net
STAR (alignment tool)	(Dobin et al., 2013)	https://github.com/alexdobin/STAR/wiki
Samtools	(Li et al., 2009)	http://www.htslib.org/
HTSeq	(Anders et al., 2015)	https://htseq.readthedocs.io/en/master/
R	NA	https://www.r-project.org/
Bioconductor	NA	https://www.bioconductor.org/
R Bioconductor package GSVA	(Hanzelmann et al., 2013)	https://anaconda.org/bioconda/bioconductor-gsva
R Bioconductor package limma	(Ritchie et al., 2015)	https://www.bioconductor.org/install/
Enrichr	(Kuleshov et al., 2016)	http://amp.pharm.mssm.edu/Enrichr/
pheatmap	N/A	https://cran.r-project.org/web/packages/pheatmap/index.html
Ingenuity pathway analysis	N/A	https://digitalinsights.qiagen.com/products-overview/discovery-insights-portfolio/analysis-and-visualization/qiagen-ipa/
Other		